Nanoscale Advances

PAPER

View Article Online
View Journal | View Issue

Check for updates

Cite this: *Nanoscale Adv.*, 2026, **8**, 2306

Numerical analysis and performance optimization of poly(3-hexylthiophene):polynaphthalene-bithiophene heterostructure device using SCAPS-1D simulation

Md. Nasir Uddin[a] and Nazia Chawdhury*[b]

A detailed numerical investigation on a P3HT:N2200 bulk heterojunction (BHJ) organic photovoltaic device was carried out using the one dimensional Solar Cell Capacitance Simulator (SCAPS-1D) tool to analyze the impact of materials and physical parameters on overall photovoltaic device performance. For the simulation analysis, we employed the photovoltaic device architecture of ITO/PEDOT:PSS/P3HT:N2200/BCP/Al, where PEDOT:PSS and BCP were used as the hole transport layer (HTL) and electron transport layer (ETL), respectively. For the comparison between BHJ and bilayer structured devices, a bilayer photovoltaic device was modelled using P3HT and N2200 semiconducting polymers as donor and acceptor layers, respectively. The superior performance of the BHJ device compared to the bilayer structured configuration motivated to focus our further investigation on the BHJ architecture. The physical and electrical parameters such as thickness, bandgap, electron and hole mobility, electron affinity, and doping density both for donor and acceptor types of the P3HT:N2200 BHJ layer were systematically varied to inspect their impact on the photovoltaic parameters. Furthermore, the role of interface defect densities at the HTL/P3HT:N2200 layer and P3HT:N2200/ETL interfaces was investigated. Additionally, the impact of bulk defect density at the P3HT:N2200 layer was investigated. Finally, the roles of operating temperature and series and shunt resistance were also studied. The simulated BHJ device exhibited a J_{SC} of 15.029 mA cm^{-2}, V_{OC} of 0.699 V, FF of 74.684% and PCE of 7.845%, whereas the bilayer structured device showed a PCE of 1.79% only with 5.952 mA cm^{-2} short circuit current density. Simulation results reveal that increasing the thickness of the P3HT:N2200 layer from 50 nm to 500 nm significantly improves the overall device PCE. Following systematic optimization of the physical and electrical parameters of the P3HT:N2200 BHJ layer, the optimized device exhibited photovoltaic device parameters of J_{SC} = 19.573 mA cm^{-2}, V_{OC} = 1.092 V, FF = 55.371% and PCE = 11.834%.

Received 28th July 2025
Accepted 23rd January 2026

DOI: 10.1039/d5na00721f

rsc.li/nanoscale-advances

1. Introduction

In recent years, industry and academia have shown intense interest in solar cells that turn sunlight into energy since they are the most significant devices for using sustainable energy to support societal advancement and lessen the impact of pollution on the environment. The flexibility in organic solar cells (OSCs) has made them a widespread area of study and attracted researchers with different backgrounds such as chemistry, physics, materials science, and even engineering. Additionally, OSCs have developed rapidly in recent years thanks to multidisciplinary collaboration, offering a power conversion efficiency (PCE) of more than 18%.[1–3] Organic photovoltaic (OPV) devices exhibit superior characteristics such as being lightweight, easy to carry and install, cost effective compared to traditional photovoltaics and the devices being flexible to be used on surfaces. Preparation of OPVs is better for the environment because it involves less energy consumption and fewer harmful materials. The duration that a photovoltaic system takes to generate the same amount of energy that was embodied in its materials and consumed during its manufacturing process is known as the energy payback time (EPBT).[4] They also produce energy quickly (short energy payback time), and therefore these repay the energy used to make them in a short time.[5,6] OPV devices exhibit a short EPBT due to their low temperature solution processing, ultrathin active layers, light weight and energy efficient roll-to-roll fabrication, which collectively minimize the energy input required for device manufacturing.[7] The bulk heterojunction (BHJ) architecture in organic photovoltaics (OPVs) enhances the donor–acceptor interfacial area relative to planar heterojunction structures,

---

[a] Department of Physics, Mawlana Bhashani Science and Technology University, Santosh, Tangail-1902, Bangladesh

[b] Department of Physics, Shahjalal University of Science and Technology, Sylhet-3114, Bangladesh. E-mail: nc-phy@sust.edu

thereby facilitating more efficient exciton dissociation and yielding higher short circuit current.[8,9] As the excitons have short diffusion lengths (∼10 nm),[10] fine morphology in the BHJ confirms that the maximum number of excitons towards the donor–acceptor interface move fast and efficiently separate into free charge carriers. In many studies, the commonly adopted BHJ structure employs poly(3-hexylthiophene) (P3HT), which is used as the donor type material, while fullerene and its derivatives, non-fullerene organic compounds and polymers are used as the acceptor type material.[11–13] Poly(3-hexylthiophene) is often paired with either fullerene or non-fullerene acceptors within bulk heterojunction (BHJ) architectures. In the field of organic electronics, fullerenes and their derivatives, such as $PC_{61}BM$ and $PC_{71}BM$, are among the most commonly employed electron acceptor materials. The power conversion efficiency of bulk heterojunction (BHJ) solar cells employing non-fullerene acceptors has now reached approximately 15%, highlighting significant progress in organic photovoltaic performance.[14,15]

N-type semiconducting polymers are crucial for balanced charge transport in organic electronics. These polymers represent a group of organic materials specifically developed to facilitate electron transport and are crucial components in a range of organic electronic applications, such as organic photovoltaics (OPVs), organic field-effect transistors (OFETs), and thermoelectric systems. The N-type semiconducting materials are able to accept electrons due to their strong electron affinity,[16,17] which supports efficient electron intake and conduction. Good example of N-type acceptor polymers include the naphthalene diimide (NDI) based polymer, poly{[*N*,*N*′-bis(2-octyldodecyl)naphthalene-1,4,5,8-bis(dicarboximide)-2,6-diyl]-*alt*-5,5′-(2,2′-bithiophene)}, simply referred to as P(NDI2OD-T2),[18] along with derivatives of perylene diimide (PDI) and benzimidazobenzothiadiazole (BBT).[19]. The (P(NDI2OD-T2)) polymer is also known as polynaphthalene bithiophene (N2200). Liu *et al.* reported 18.22% power conversion efficiency (PCE) for a single junction BHJ solar cell device using a non-fullerene acceptor.[3] This significant enhancement of the device efficiency highlights the advancements in non-fullerene acceptors (NFAs), demonstrating their potential to enhance photo absorption capabilities, exciton generation, optimization of energy level alignment, efficient exciton dissociation into free charges and charge transport within the organic photovoltaic devices. Xu *et al.* reported that the PCE of an organic solar cell device with P3HT and a non-fullerene acceptor can be improved from 6.62% to 8.25% by an environmentally friendly solvent processing method.[20] A significantly improved result was shown by Yang *et al.* with a power conversion efficiency of 9.46%, by introducing a new non-fullerene acceptor, which has energy levels well-matched to those of the P3HT polymer, enabling favorable surface morphology through precise molecular packing.[21] Recent studies reported that the power conversion efficiency of P3HT:NFA BHJ solar cells has exceeded 10%, indicating a major advancement in polymer:polymer solar cells.[22]

The advancement in organic photovoltaic performance can be attributed to considerable progress in the field of materials science and engineering, which together have made it possible to develop more efficient and stable device architectures. Numerous studies have demonstrated that the performance of organic photovoltaics is highly dependent on the thickness of the donor:acceptor layer within the photoactive bulk heterojunction.[23,24] As the thickness increases, more light can be absorbed, which enhances exciton generation and can lead to a higher short circuit current density (J_{SC}). Bakour and colleagues concluded that the concentration as well as the thickness of the active layer has a great impact on the performance of the photovoltaic device.[25] They also added that the variations in the thickness of the active layer have a significant effect on light absorption and charge carrier dynamics, thus affecting key performance parameters of the device such as the open circuit voltage (V_{OC}), short circuit current density (J_{SC}), fill factor (FF), and power conversion efficiency (PCE). Thus, both the thickness and concentration optimization of the active layer are essential to maximize the device efficiency. Again, the device performance is critically influenced by intrinsic material properties such as bandgap, dielectric constant, and electron affinity. The bandgap determines the spectral range of light absorption;[26] a narrower bandgap enables the harvesting of lower photon energy, resulting in improved J_{SC}. However, an excessively narrow bandgap can lead to a decline in device V_{OC},[27] therefore an optimum bandgap of the active layer is crucial as it balances efficient photon absorption with sufficient voltage output to maximize the overall power conversion efficiency (PCE) of the device.[28] The dielectric constant of a material is a key factor in reducing the recombination of photogenerated electron–hole pairs by enhancing the separation of charge carriers and reducing their mutual coulombic attraction.[29,30] It affects the exciton binding energy; higher dielectric constants facilitate exciton dissociation into free charge carriers, enhancing charge generation efficiency and reducing recombination losses.[31] Even so, increasing the dielectric constant of the active layer leads to higher trap density and greater energetic disorder, which may have a detrimental effect on the device performance.[32] The energy level alignment between the donor and acceptor materials is greatly influenced by the electron affinity of the active layer, which also has an effect on the efficiency of charge transfer processes. Appropriate alignment ensures efficient electron extraction resulting in higher V_{OC}, while misalignment increases recombination rates, thereby causing energy losses.[33] The introduction of buffer layers or interfacial layers between the BHJ active layer and electrode interfaces can improve the performance of the organic photovoltaic device by ensuring efficient charge extraction, minimizing interfacial recombination, and optimizing the energy level alignment.[34,35] The two types of interfacial layers such as the electron transporting layer (ETL) and hole transporting layer (HTL) are usually used in organic photovoltaics to reduce the recombination rate by enabling selective transport of one type of carrier (electron or hole), while blocking the other.[36,37] Poly(3,4-ethylenedioxythiophene):poly(styrene) (PEDOT:PSS) is a commonly used hole transport layer in optoelectronic devices due to its high electrical conductivity, optical transparency, and promising energy level alignment with donor materials. It facilitates efficient hole extraction, reduces interfacial recombination, and improves the surface morphology of the underlying ITO electrode.[38,39] Bathocuproine (BCP) is frequently employed as an interfacial layer in polymer solar cells, serving both as an electron transport layer and a hole blocking layer.[40,41] It is generally inserted between the active layer and the metal cathode, where it promotes effective electron extraction and inhibits the movement of holes toward the cathode, thus reducing interfacial charge recombination. Additionally, proper energy level alignment between the active layer and the cathode is ensured by introducing the BCP layer, resulting in improved charge carrier transport that enhances the overall device PCE.[42–44]

To date, only a limited number of experimental studies on P3HT and N2200 polymers have shown that the power conversion efficiency is relatively very low. Guozheng *et al.* reported that an additive-assisted thermal annealing process on the P3HT:N2200 solar cell improves the device PCE from 0.17% to 0.65%.[45] Also, Huajun *et al.* studied the performance of a ternary blend photovoltaic device using P3HT, N2200 and SiNc dye. They reported that the device PCE can be improved from 0.82% to 1.4% only after the addition of SiNc dye.[46] In our recently published work, we experimentally fabricated a P3HT:N2200 BHJ organic photovoltaic device. Consistent with the other reported results our results exhibit a relatively very low device PCE of 0.36%.[11] The present work is only concerned with the simulation of the organic photovoltaic device based on the P3HT and N2200 polymers in bilayer and bulk heterostructure systems, utilizing the Solar Cell Capacitance Simulator (SCAPS-1D) software. The primary objective of this work is to conduct a comprehensive analysis of the key parameters that govern the performance of the devices. In particular, the study focuses on enhancing the power conversion efficiency (PCE) by systematically modifying the physical and electronic properties of the photo-active layer. Through detailed simulations, this investigation aims to explicitly assess the impact of these modifications on the overall operational efficiency, charge transport dynamics, and energy level alignment within the device architecture. This research also includes the impact of defect density in the active layer as well as defects at the layer interfaces. Finally, the effect of working point temperature on photovoltaic properties has been studied.

Our simulation can act as a tool to explain phenomena observed in the literature. For example, the work by Zhang *et al.*[47] demonstrated that annealing below P3HT's melting point leads to a face-on orientation and an interpenetrating network, while annealing above it leads to edge-on P3HT and hierarchical phase separation. We can model these scenarios by adjusting carrier mobility anisotropies and the effective interfacial area in our BHJ simulation. By correlating these simulated morphological parameters with performance metrics like internal quantum efficiency (IQE) and external quantum efficiency (EQE), we offer a quantitative physics-based explanation for why one morphology outperforms the other. Also, the study by Xu *et al.*[46] found that the sensitizer SiNc10 outperforms SiNc6 due to better distribution at the P3HT:N2200 interface, preventing large aggregates. In a simulation framework, we can model this by introducing a third, sensitizing material layer or a region with specific optical and electronic properties and studying the effect of its positioning (dispersed *vs.* aggregated) on charge generation and recombination. This creates a bridge between complex morphological analysis and its direct consequences.

2. Materials and simulation methods

Fig. 1 illustrates the organic semiconducting materials used for the proposed bilayer and bulk-heterojunction organic photovoltaic (OPV) device simulation. In the bulk-heterojunction architecture, a blend of P3HT and N2200 polymers is employed.

For device modeling and numerical analysis, the Solar Cell Capacitance Simulator (SCAPS) version (3.3.12) has been used. It is a one-dimensional windows oriented solar cell simulation program designed by the Department of Electronics and Information Systems (ELIS), the University of Ghent, Belgium.[48–50] SCAPS is a flexible simulation tool that allows users to model a device's current density–voltage (J–V) behavior as well as the quantum efficiency (QE) spectrum. It accomplishes this by numerically solving the core semiconductor equations, such as the Poisson equation and the electron and

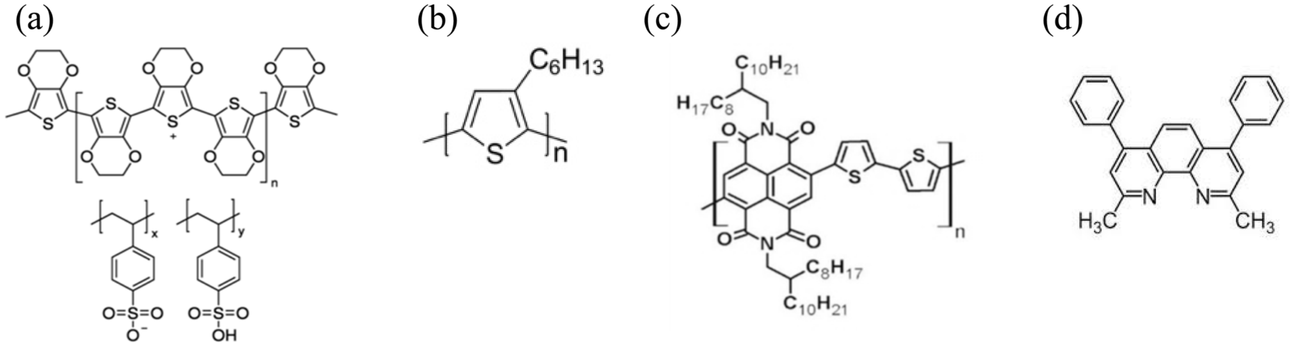

Fig. 1 Chemical structure of (a) PEDOT:PSS, employed as the hole-transporting and electron-blocking layer; (b) poly(3-hexylthiophene) (P3HT), which serves as the donor polymer; (c) polynaphthalene bithiophene (N2200), used as the acceptor polymer; and (d) bathocuproine (BCP) materials for the hole-blocking and electron-transporting layer.

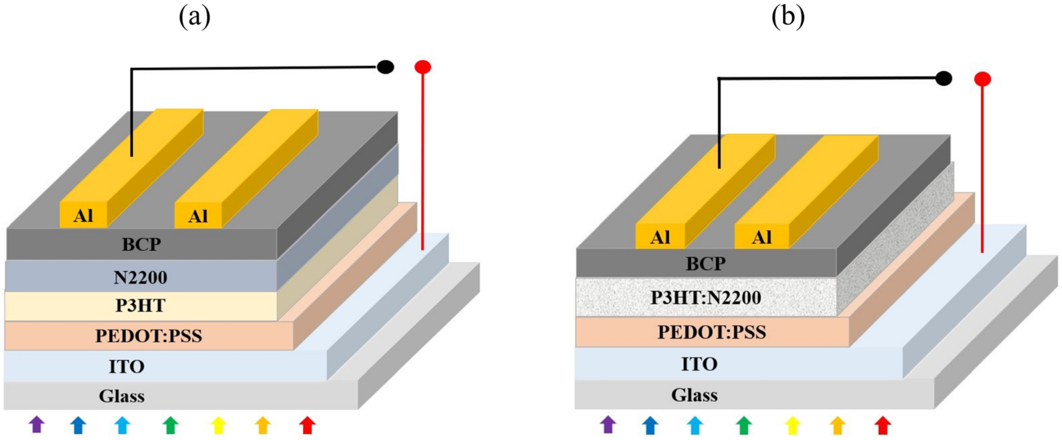

Fig. 2 Device architecture of (a) bilayer and (b) bulk-heterojunction photovoltaic devices for SCAPS simulation.

hole continuity equations.[51–53] The solutions of the following three coupled, nonlinear differential equations facilitate the extraction of the solar cell's electrical parameters.

$$\frac{\mathrm{d}}{\mathrm{d}x}\left(-\varepsilon(x)\,\frac{\mathrm{d}\Psi}{\mathrm{d}x}\right) = q[p(x) - n(x) + N_{\mathrm{D}}{}^{+}(x) - N_{\mathrm{A}}{}^{-}(x)] \tag{1}$$

$$\frac{\delta J_{\mathrm{n}}}{\delta x} = q\left(R_{\mathrm{n}} - G + \frac{\delta n}{\delta t}\right) \tag{2}$$

$$\frac{\delta J_{\mathrm{p}}}{\delta x} = -q\left(R_{\mathrm{p}} - G + \frac{\delta p}{\delta t}\right) \tag{3}$$

The electric field and space charge density within a p–n junction are governed by Poisson's equation which is expressed by eqn (1). In this equation, $\varepsilon(x)$ denotes the material permittivity, q represents the elementary charge, Ψ signifies the electrostatic potential, $n(x)$ denotes the total electron density, $p(x)$ corresponds to the total hole density, and $N_{\mathrm{D}}{}^{+}(x)$ and $N_{\mathrm{A}}{}^{-}(x)$ indicate the ionized donor-like and ionized acceptor-like doping concentrations. In the continuity equations displayed in eqn (2) and (3), J_{n} and J_{p} symbolize the current densities of electrons and holes, respectively, where, R_{n} and R_{p} are the recombination rates for electrons and holes, respectively, and G denotes the generation rate. In semiconductor materials, current generation results from the movement of charge carriers due to the presence of an electric field (drift current) or a carrier concentration gradient (diffusion current).[54] The carrier current densities can be rewritten as follows:[55,56]

$$J_{\mathrm{n}} = qn\mu_{\mathrm{n}}E + qD_{\mathrm{n}}\frac{\delta n}{\delta x} \tag{4}$$

$$J_{\mathrm{p}} = qp\mu_{\mathrm{p}}E + qD_{\mathrm{p}}\frac{\delta p}{\delta x} \tag{5}$$

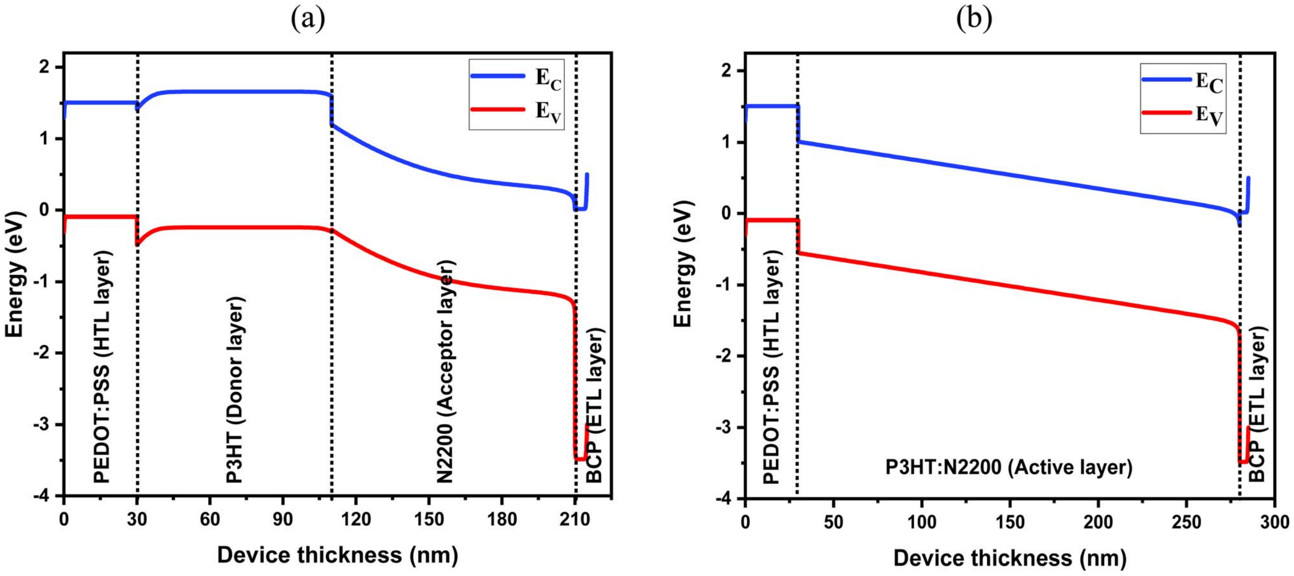

Fig. 3 Energy band diagram of (a) bilayer and (b) bulk-heterojunction photovoltaic devices after contact.

Table 1 Input parameters of each layer for SCAPS simulation

Parameters	PEDOT:PSS[34,61]	P3HT	N2200	P3HT:N2200	BCP[62]
Thickness (nm)	30 [varied]	80 [varied]	100 [varied]	250 [varied]	5 [varied]
Band gap (eV)	1.6	1.9 (ref. 63)	1.47 (ref. 64 and 65)	1.56 (ref. 11)	3.5
Electron affinity (eV)	3.4	3.5 (ref. 66 and 67)	3.9 (ref. 16 and 64)	3.9 (ref. 14)	3.7
Dielectric permittivity, (ε_r)	3	4.4 (ref. 66 and 67)	3.2 (ref. 68)	3.8 (ref. 57 and 58)	10
CB effective density of states (cm^{-3})	1×10^{22}	1×10^{22} (ref. 34)	1×10^{22}	1×10^{18}	1.8×10^{21}
VB effective density of states (cm^{-3})	1×10^{22}	1×10^{22} (ref. 34)	1×10^{22}	1×10^{19}	2.2×10^{21}
Electron thermal velocity ($cm\ s^{-1}$)	1×10^{7}	1×10^{7}	1×10^{7}	1×10^{7}	1×10^{7}
Hole thermal velocity ($cm\ s^{-1}$)	1×10^{7}	1×10^{7}	1×10^{7}	1×10^{7}	1×10^{7}
Electron mobility ($cm^2\ V^{-1}\ s^{-1}$)	4.5×10^{-4}	10 (ref. 63, 69 and 70)	8.5×10^{-1} (ref. 71)	1.6	2×10^{-2}
Hole mobility ($cm^2\ V^{-1}\ s^{-1}$)	9.9×10^{-5}	2.8 (ref. 63, 69 and 70)	3.4×10^{-6} (ref. 72)	1.6	1×10^{-3}
Shallow uniform donor density (cm^{-3})	0	0	1×10^{16}	0	1×10^{21}
Shallow uniform acceptor density (cm^{-3})	3×10^{20} (ref. 73 and 74)	1×10^{18} (ref. 69)	0	0	1×10^{10}
Defect density (cm^{-3})	1×10^{14} (ref. 73 and 74)	1×10^{16} (ref. 69)	1×10^{14}	1×10^{12}	1×10^{17}

Here, μ_n and μ_p represent the mobilities of electrons and holes, respectively, while D_n and D_p denote their corresponding diffusion coefficients. E stands for the electric field. The multilayer structures of the two devices were modeled using structural components, specifically including ITO coated glass/PEDOT:PSS/P3HT/N2200/BCP/Al as the bilayer structure (device 1) shown in Fig. 2(a) and ITO coated glass/PEDOT:PSS/P3HT:N2200/BCP/Al as the bulk-heterojunction structure (device 2) shown in Fig. 2(b). Fig. 3(a) and (b) shows the energy band diagram of the bilayer and bulk-heterojunction structured devices, respectively, after contact. Table 1 presents the fundamental parameters of each layer, derived from previously published studies. The thermal velocities of electrons and holes are assumed to be identical (1×10^7 cm s^{-1}) across all layers. The band gap of the P3HT:N2200 layer (1.56 eV) was determined using the Tauc plot based on our previously published UV-vis absorption data of the P3HT:N2200 film.[11] The absorption spectrum of the P3HT:N2200 active layer was generated using the inbuilt Tauc-Lorentz optical model within SCAPS-1D. This model constructs the absorption coefficient profile based on the input bandgap and dielectric properties. The dielectric permittivity, (ε_r) of the P3HT:N2200 layer is calculated by averaging the permittivity values of the donor and acceptor materials.[57,58] As no experimental and theoretical values are available for carrier mobility of the P3HT:N2200 system in the existing literature, we initially used a mobility of 1.6 cm^2 V^{-1} s^{-1} as a placeholder to probe the upper performance limit of a polymer:polymer photovoltaic device.[14] A uniform defect density of 1×10^{16} cm^{-2} was assumed for various interfaces such as: PEDOT:PSS/P3HT; P3HT:N2200; and N2200/BCP in the bilayer structure and PEDOT:PSS/P3HT:N2200 and P3HT:N2200/BCP in the bulk-heterojunction structure. Here, the electron and hole capture cross section of all interface layers was kept as 1×10^{-15} cm^{-2}. Indium-doped tin oxide (ITO) and aluminium were selected as the front and back contacts, respectively. The work functions of ITO and Al were set to 4.7 eV and 4.2 eV, respectively.[59,60] The input parameters of the interface layers are kept uniform to make it easier to compare how changes in other factors affect the device performance.

3. Results and discussion

3.1. P3HT/N2200 bilayer photovoltaic device

Photovoltaic cells operate by converting incident light energy into electrical current. Under dark conditions or when the device is not exposed to light, all photovoltaic devices operate as large-area diodes, displaying an exponential current density–voltage (*J*–*V*) behavior.[75] Upon illumination, the incident light provides enough energy to create excitons within the photoactive material.[76] These generated excitons dissociate into free charge carriers and then move through the device, initiating the photovoltaic process. The current density–voltage (*J*–*V*) characteristics and quantum efficiency (QE) spectrum of the P3HT/N2200 bilayer photovoltaic device are shown in Fig. 4(a) and (b), respectively. The *J*–*V* characteristics exhibit a maximum power conversion efficiency (PCE) of 1.79%, an open circuit voltage (V_{OC}) of 0.575 V and a fill factor (FF) of 52.293%, with a short circuit current density (J_{SC}) of 5.952 mA cm^{-2}. A broadened quantum efficiency (QE) spectrum within the visible region is shown in Fig. 4(b) with maximum 12.8% QE at 660 nm wavelength due to the stronger absorption by the active layer (P3HT/N2200).[77] Beyond this wavelength, the QE drops because the absorption coefficient of the active layer decreases at longer wavelengths, resulting in fewer photogenerated excitons and reduced carrier collection.

3.2. P3HT:N2200 bulk heterojunction photovoltaic device

The *J*–*V* characteristics and QE spectrum of the P3HT:N2200 bulk heterojunction photovoltaic device are shown in Fig. 5(a) and (b), respectively. The *J*–*V* characteristics exhibit a maximum PCE of 7.845%, V_{OC} of 0.699 V and FF of 74.684%, with a J_{SC} of 15.029 mA cm^{-2}. A broadened QE spectrum within the visible region is shown in Fig. 5(b) with maximum 64.44% QE at 470 nm wavelength indicating effective photo absorption and electrical energy conversion across a wide range of wavelengths, specifically in the blue region. After that the QE spectrum starts to decline slowly and reaches zero at a wavelength of 800 nm due to the poor absorption by the P3HT:N2200 active layer at longer wavelengths. The comparison of the *J*–*V* characteristics

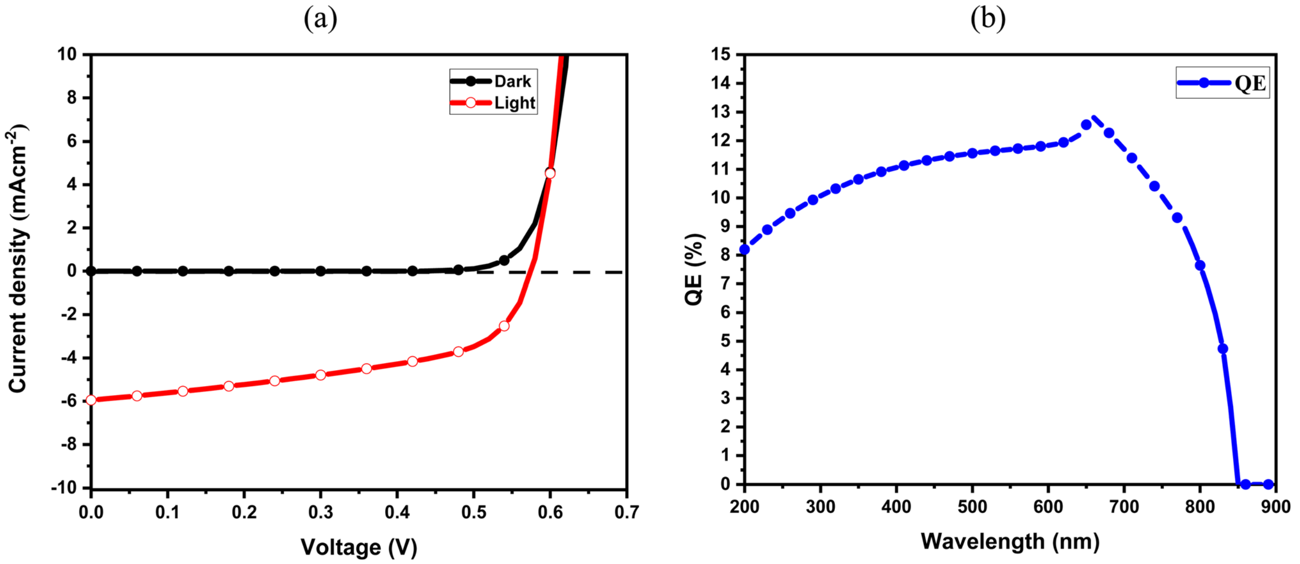

Fig. 4 (a) Current density–voltage (J–V) characteristics in the dark and after illumination; (b) QE spectrum of the P3HT/N2200 bilayer photovoltaic device.

between bilayer and bulk heterojunction devices reveals a significant difference in their performance metrics, specifically, in the PCE of the devices. In the case of the bulk heterojunction structure more efficient exciton dissociation and charge transport occur due to its larger interfacial area and optimized nanoscale morphology. This results in higher photocurrent generation and an improved device PCE compared to the bilayer device architecture.[78]

3.3. Impact of P3HT (donor) and N2200 (acceptor) layer thickness on the photovoltaic performance of the bilayer structured photovoltaic device

The performance of organic photovoltaics is significantly affected by the thickness of donor and acceptor layers. Therefore, optimum thicknesses of these layers are crucial to enhance the device efficiency, photoresponsivity, and overall performance metrics.[79] Zhang *et al.* reported that a specific thickness ratio of donor and acceptor layers can lead to a considerable improvement in the performance of organic photovoltaic devices.[24] It has been reported that an optimal thickness of 500 nm was found to maximize the device performance, while thicknesses beyond this value led to a decrease in the short circuit current density and fill factor of PM6:Y6 BHJ-based organic solar cells.[80] The J–V characteristics of the P3HT/N2200 bilayer photovoltaic device are shown in Fig. 6(a) and (b), respectively, by changing the thicknesses of P3HT and N2200 layers from 10 nm to 500 nm respectively. The device performance parameters are shown in Fig. 6(c) and (d),

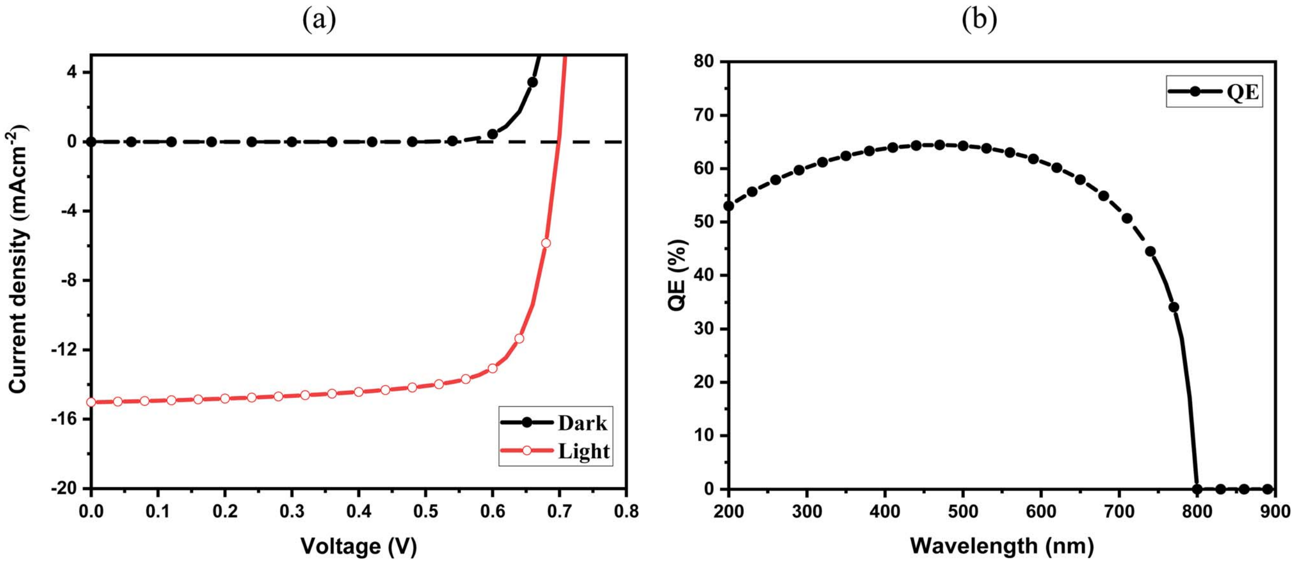

Fig. 5 (a) Current density *versus* voltage (J–V) characteristics in the dark and after illumination; (b) QE spectrum of the P3HT:N2200 bulk heterojunction photovoltaic device.

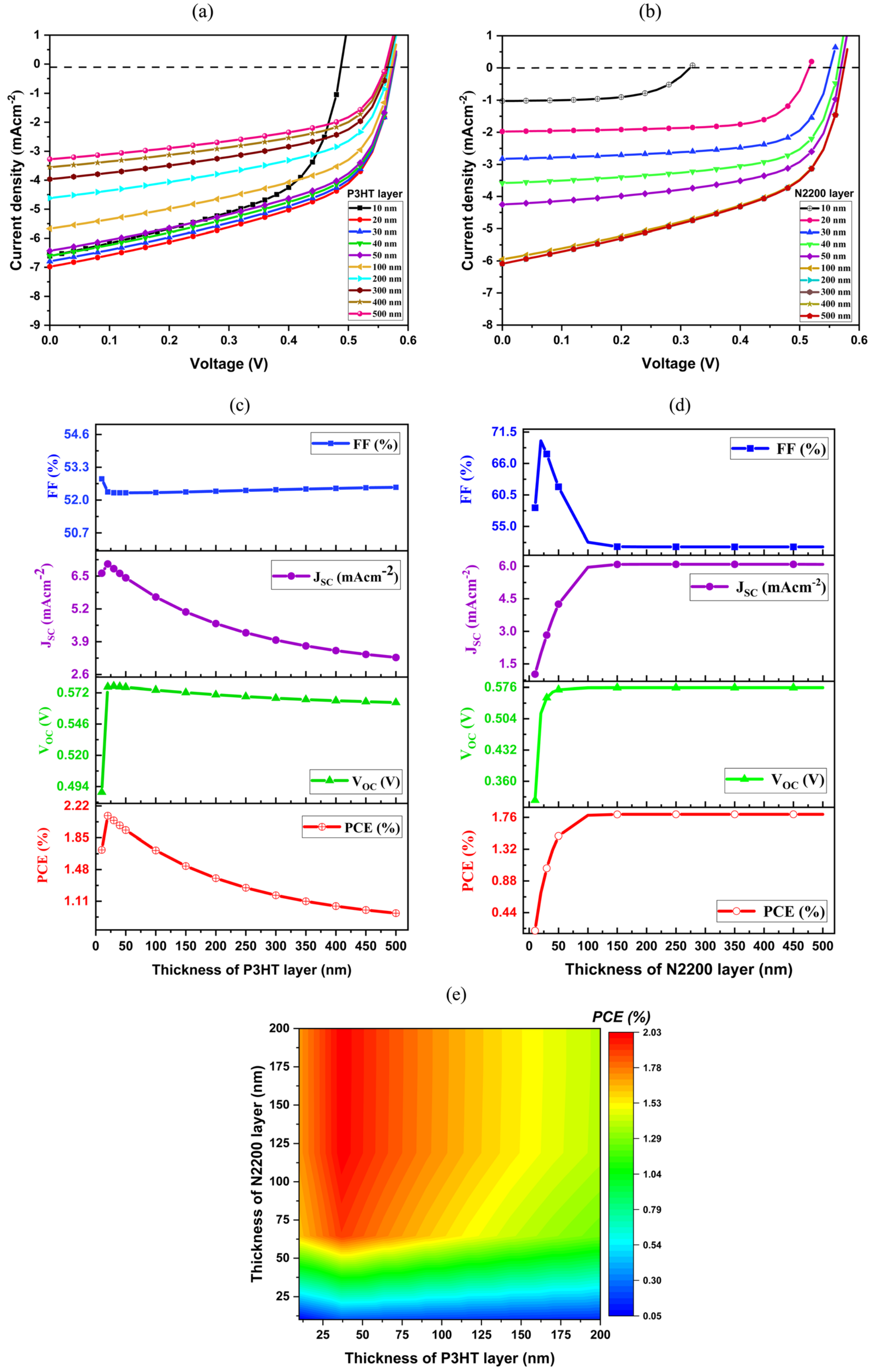

Fig. 6 *J–V* characteristics of the P3HT/N2200 bilayer device, showing the influence of thickness variation of (a) P3HT and (b) N2200 layers. The corresponding thickness dependent photovoltaic parameters are presented in (c) and (d) where (e) presents the contour plot of the combined optimum thickness for the P3HT/N2200 bilayer.

respectively, for the bilayer and bulk-heterojunction devices. For the P3HT layer, the PCE reaches a maximum of 2.11% at a thickness of 20 nm and declines gradually with further increasing thickness and then falls to 0.97% at 500 nm. Likewise, the J_{SC} approaches its highest value with a peak of 6.979 mA cm^{-2} at 20 nm and then decreases continuously as the layer thickness increases. This decrease in PCE at higher thickness primarily results from the reduced J_{SC}, which arises from the short diffusion length of the charge carriers, whereas poor PCE at the thicknesses less than 20 nm is due to the less absorption by the thin P3HT layer, which limits the exciton generation. There are no significant changes observed in the FF for the thick P3HT layer (>20 nm) due to stable resistive losses and continuous film formation, whereas the FF slightly decreases below 20 nm due to the ultrathin P3HT layer, which causes incomplete film coverage due to poor morphology. This behavior suggests that an excessively thick donor layer increases charge recombination, thereby degrading the overall device performance.[81,82] For the N2200 acceptor layer, the photovoltaic parameters demonstrate a distinct trend with increasing the thickness. The V_{OC} increases significantly from 0.316 V at 10 nm to approximately 0.575 V at 100 nm, after which it stabilizes, indicating improved junction quality and reduced leakage at sufficient thickness.[83] Likewise, the J_{SC} increases with thickness up to around 200 nm, due to enhanced light absorption and efficient exciton dissociation. Beyond this thickness, J_{SC} reaches its saturation point, implying that further increases in the acceptor layer do not contribute to additional photocurrent due to saturation in optical absorption and charge transport.[84] The FF sharply increases from 10 nm to 20 nm due to improved N2200 film formation and attains its optimum value at 20 nm. Beyond 20 nm, the FF decreases because of the probability of carrier recombination increases at higher N2200 thicknesses. Fig. 6(d) shows a gradual decline of the FF from higher values (~69.96%) at thin layers to about 51.5% at greater thicknesses, implying that thicker N2200 layers introduce increased series resistance or charge recombination losses.[85] Consequently, the PCE of the device shows a clear dependence on the thickness of the N2200 acceptor layer. The PCE increases sharply from 0.19% to 1.79% as the thickness increases from 10 nm to 100 nm due to the thicker N2200 layer, which enhances light absorption and enables improved exciton dissociation and charge collection. Beyond a thickness of about 100 nm, the PCE levels off at around 1.80% and remains unchanged up to 500 nm due to stable morphology and resistive losses. This saturation indicates that increasing the acceptor layer thickness further does not generate additional photocurrent, likely due to the limited exciton diffusion length and higher recombination losses in overly thick layers.[86,87] Chen *et al.* reported that as the thickness surpasses optimal levels, the photocurrent does not improve due to high recombination losses at the donor–acceptor interface.[88] Therefore, an optimal thickness range is identified around 150 nm to 200 nm for the N2200 layer that balances the efficient light absorption with effective charge transport and extraction.

In this thickness optimization study, the thickness of the N2200 layer was kept constant at 100 nm while the thickness of the P3HT layer was varied from 10 nm to 500 nm. Also, when the thickness of N2200 was varied from 10 nm to 500 nm, the thickness of the P3HT layer was kept constant at 80 nm. In this case, we get the best donor or acceptor thickness alone. Therefore, the final combined optimum P3HT/N2200 layer thickness is very crucial in bilayer OPV devices because it ensures maximum light harvesting, efficient exciton dissociation, balanced charge transport and overall device efficiency. Fig. 6(e) shows the contour plot indicating the combined optimum thickness of the P3HT and N2200 layers. From the contour plot the maximum PCE is observed in the reddest region which is at 35–40 nm for P3HT and >100 nm for N2200 layer. The thickness of the N2200 layer can be increased up to 200 nm, as a thicker layer enhances the device PCE, as confirmed in Fig. 6(d), which shows that the device PCE increases with increasing N2200 thickness. The previously determined optimum thickness of P3HT (20 nm) differs from the final combined optimum thickness because, in the latter case, simultaneous variation of both P3HT and N2200 layers influences each other, affecting the overall device performance.

3.4. Impact of P3HT:N2200 active layer thickness on the photovoltaic performance of the bulk heterojunction structured photovoltaic device

The thickness of the active layer in organic solar cells significantly influences their performance, affecting parameters such as power conversion efficiency, short-circuit current density, fill factor and open circuit voltage. Fig. 7(a) and (b) displays the *J–V* characteristics and QE spectra of bulk heterojunction photovoltaic devices with varying the thickness of the P3HT:N2200 active layer from 10 nm to 1000 nm within the wavelength range from 300 nm to 900 nm. The photovoltaic performance parameters are shown in Fig. 7(c). The device V_{OC} increases gradually from 0.613 volt to 0.731 volt as the thickness of the P3HT:N2200 layer increases from 50 nm to 500 nm, while J_{SC} increases significantly from 5.175 mA cm^{-2} to 18.263 mA cm^{-2}. This can be attributed to the stronger light absorption by the thicker layer, resulting in improved exciton generation and current production.[77] Nevertheless, the FF shows a continuous degradation from 79.24% to 67.67% over this range due to the increase in internal losses at thicker layers. Collectively, the device PCE reaches a maximum of 9.03% at a thickness of 500 nm. Although, the V_{OC} and J_{SC} continue to increase slightly, the FF drops more rapidly, causing the PCE to decline marginally to 7.99% at 1000 nm. This behavior underscores that while a thicker active layer enhances light harvesting, excessive thickness can deteriorate charge extraction and reduce overall device performance due to enhanced recombination and limited charge carrier mobility.[89] From Fig. 7(c), it can be observed that the device achieves a PCE of approximately 4.56% at the thickness of 100 nm of the P3HT:N2200 layer.

The QE spectra of these bulk heterojunction devices demonstrate a clear dependence on the active layer thickness across the examined wavelength range of 200 nm to 900 nm, shown in Fig. 7(b). At shorter wavelengths (200–300 nm), the QE gradually increases with increasing thickness, reflecting

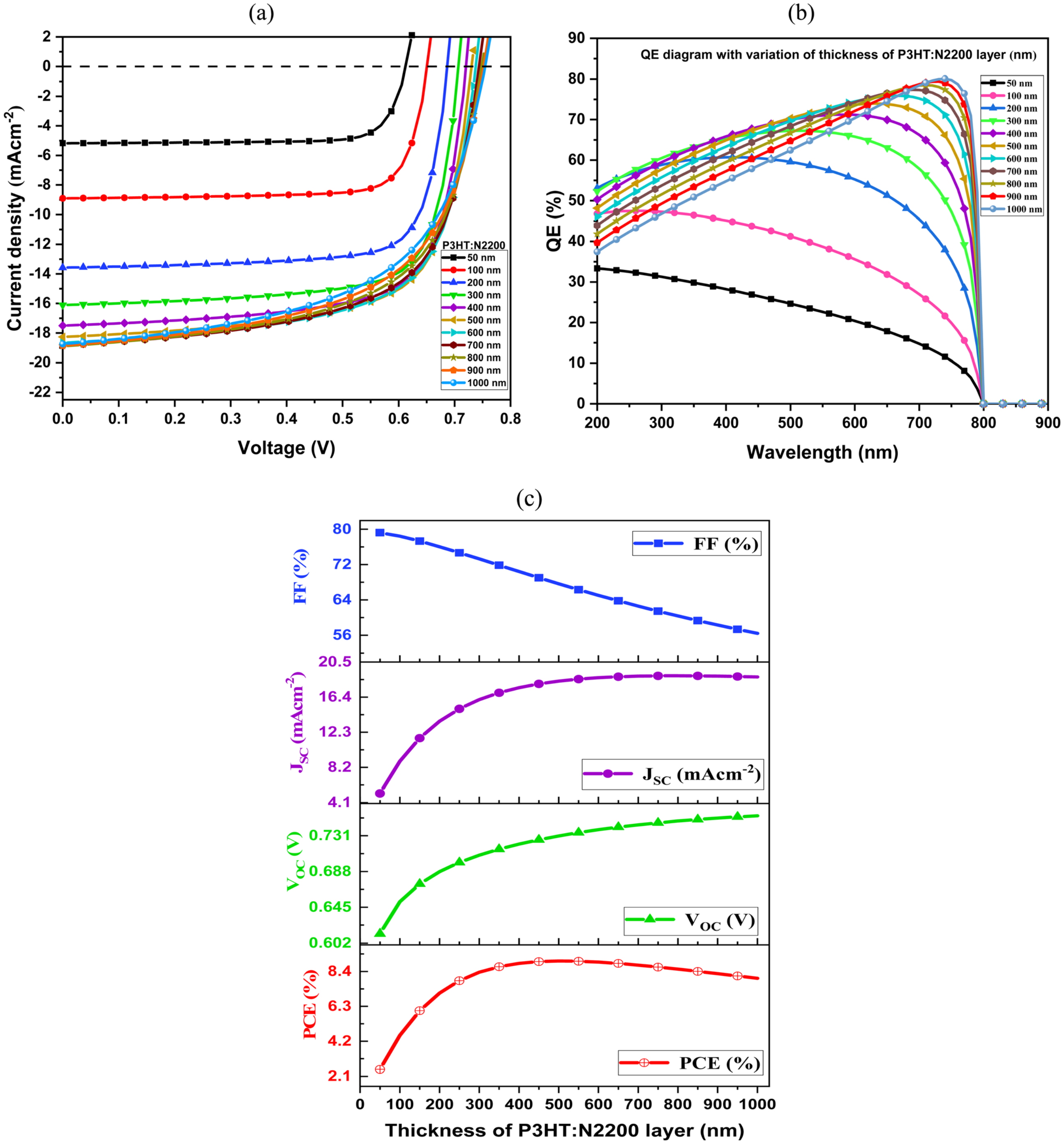

Fig. 7 (a) J–V characteristics of the bulk heterojunction device with varying thicknesses of the P3HT:N2200 active layer; (b) quantum efficiency (QE) spectra at different P3HT:N2200 layer thicknesses; and (c) the corresponding thickness-dependent photovoltaic parameters.

enhanced photon absorption due to a longer optical path and improved exciton generation. As the wavelength shifted into the visible region (400–700 nm), the QE value significantly increases at higher thickness with peak values 70–79% from 500 nm to 1000 nm. This suggests that the thicker active layers can more effectively capture a broader portion of the incident light spectrum, which contributes to the increased J_{SC} observed in the corresponding J–V data. However, at longer wavelengths beyond ~700 nm, the QE spectra tend to saturate and slightly decrease, especially for the thinnest layers, due to limited absorption depth and insufficient material to fully harvest longer wavelength photons. Notably, extremely thin active layers (50–100 nm) exhibit significantly lower QE across the spectrum, confirming that insufficient layer thickness limits light absorption. At wavelengths above about 800 nm, the QE drops to almost zero for all thicknesses, because the light does not have enough energy to be absorbed by the P3HT:N2200 layer.

Apart from the absorption characteristics of photons, the degree of interfacial recombination and density of interfacial defects critically influence the overall QE response.[90] When the active layer is too thin (*e.g.*, 50–100 nm), the photogeneration occurs very close to the HTL/absorber and ETL/absorber interfaces. Charge carrier extraction becomes easier as the electrons and holes travel a short distance but the J_{SC} is low as the layer is too thin to absorb a significant portion of incident photons, especially long wavelength photons. However, because the photogenerated carriers are very close to the interfaces (HTL/absorber and ETL/absorber), the recombination at the interfaces is dominant. This enhances the leakage current, which reduces the device V_{OC}. Also, the thin layer reduces bulk recombination as well as offers less series resistance leading to a higher FF due to the short travel distance of the charge carriers. That is why, the *J*–*V* curve shows lower J_{SC} and V_{OC} (Fig. 7(a)), which degrades the overall device PCE, shown in Fig. 7(c). QE is poor, particularly at longer wavelengths, originating from recombination at the poor ETL/absorber interface and due to limited photon absorption by the thin active layer. As the thickness increases from 200–1000 nm, the QE maxima shifted towards the higher wavelength due to the dominance of HTL/absorber interfacial recombination. After that QE decreases from its maxima at the longer wavelength where trap assisted carrier recombination increases due to a longer transport path and ETL/absorber interfacial recombination. In the thickness range of 200–300 nm, absorption occurs more uniformly across the P3HT:N2200 layer, which represents a balance where both interfaces (HTL/absorber and ETL/absorber) support efficient carrier extraction, as electron diffusion length is sufficient to reach the respective interfaces from anywhere in the absorber layer. Therefore, there is an improvement in J_{SC} and V_{OC}, but the FF decreases as the series resistance increases because of the thick layer.[91]

3.5. Impact of working point temperature on the photovoltaic performance of P3HT/N2200 bilayer and P3HT:N2200 bulk heterojunction structured photovoltaic devices

The working point temperature has a significant effect on the performance of photovoltaic devices by impacting charge transport, recombination process, and the overall stability of the device.[92] The performance of both the bilayer and bulk heterojunction devices as a function of working point temperature is shown in Fig. 8(a) and (b), respectively. As the working point temperature increases from 290 K to 500 K, the power conversion efficiency (PCE) of the bilayer device drops sharply from 1.90% at 290 K to nearly zero at 500 K. This significant drop is mainly due to a continuous decrease in open-circuit voltage from 0.608 V to near 0 V due to the increase in reverse saturation current density at elevated temperature and a moderate decline in short circuit current density from 6.03 mA cm^{-2} to 3.56 mA cm^{-2}. The FF reduces from 52% to 0%, indicating loss in device performance. However, the PCE of the bulk heterojunction device decreases gradually from 8.1% to 2.7% at working point temperature from 290 K to 500 K respectively. The V_{OC} rapidly decays from 0.72 V to 0.32 V, and the J_{SC} drops from 15.06 mA cm^{-2} to 14.19 mA cm^{-2}, indicating better photogeneration and collection despite the elevated temperatures. The FF of the bulk heterojunction structure is decreasing from about 75% to 58% at elevated temperature attributed to increased carrier recombination and thermally activated trap states, which collectively reduce the charge extraction efficiency and distort the *J*–*V* characteristics near the maximum power point.

Overall, an increase in operating temperature results in reduced performance for both device architectures. In most PV cells, when temperature increases the J_{SC} usually increases slightly. In our simulation, the observed decrease in J_{SC} is indeed a deviation from the behavior of conventional solar cells. We attribute this primarily to the dominance of temperature-activated trap-assisted recombination. An increase in operating temperature supplies extra thermal energy to the charge carriers. As a result, electrons gain more kinetic energy and are more prone to recombine with holes before arriving at the electrodes.[93] This enhanced recombination at higher temperatures leads to the observed reduction in J_{SC}. Furthermore, the conductivity of the material is degraded at elevated temperature due to increased charge carrier scattering from lattice vibrations (phonons).[94] Therefore, higher temperatures lead to greater thermal excitation, which in turn causes a drop in device performance. As the carrier recombination rates increase with temperature, more charge carriers recombine before they reach the depletion region, not contributing to current generation.[25] But the results demonstrate that the bulk heterojunction device is more thermally robust than the bilayer device, exhibiting higher PCE, V_{OC}, J_{SC}, and FF throughout the temperature range. As this study demonstrates that the bilayer device delivers a significantly lower power conversion efficiency (1.79%) than the bulk heterojunction structure (9.03%), the bulk heterojunction architecture has been chosen as the main focus for our subsequent numerical analyses.

3.6. Impact of donor type (N_D) and acceptor type (N_A) doping densities on the photovoltaic performance of the P3HT:N2200 bulk heterojunction structured photovoltaic device

For bulk heterojunction structured photovoltaic devices, the donor type (N_D) and acceptor type (N_A) doping densities in the donor:acceptor layer significantly affect the device performance. Therefore, optimization of the N_D type and N_A type doping densities in the P3HT:N2200 layer is essential to achieve better device performance. Initially, both the doping densities were intentionally kept at 0 cm^{-3} to accurately represent the intrinsic nature of P3HT:N2200. When N_A was varied, N_D was kept fixed at 0 cm^{-3}, and when N_D was varied, N_A was kept fixed at 0 cm^{-3}. Fig. 9 shows how N_D type and N_A type doping densities in the P3HT:N2200 layer effect photovoltaic matrices. Doping densities of the P3HT:N2200 layer have been varied from 10^{12} cm^{-3} to 10^{18} cm^{-3}. It has been observed that the photovoltaic parameters such as V_{OC}, J_{SC}, FF and PCE remain constant up to 10^{14}

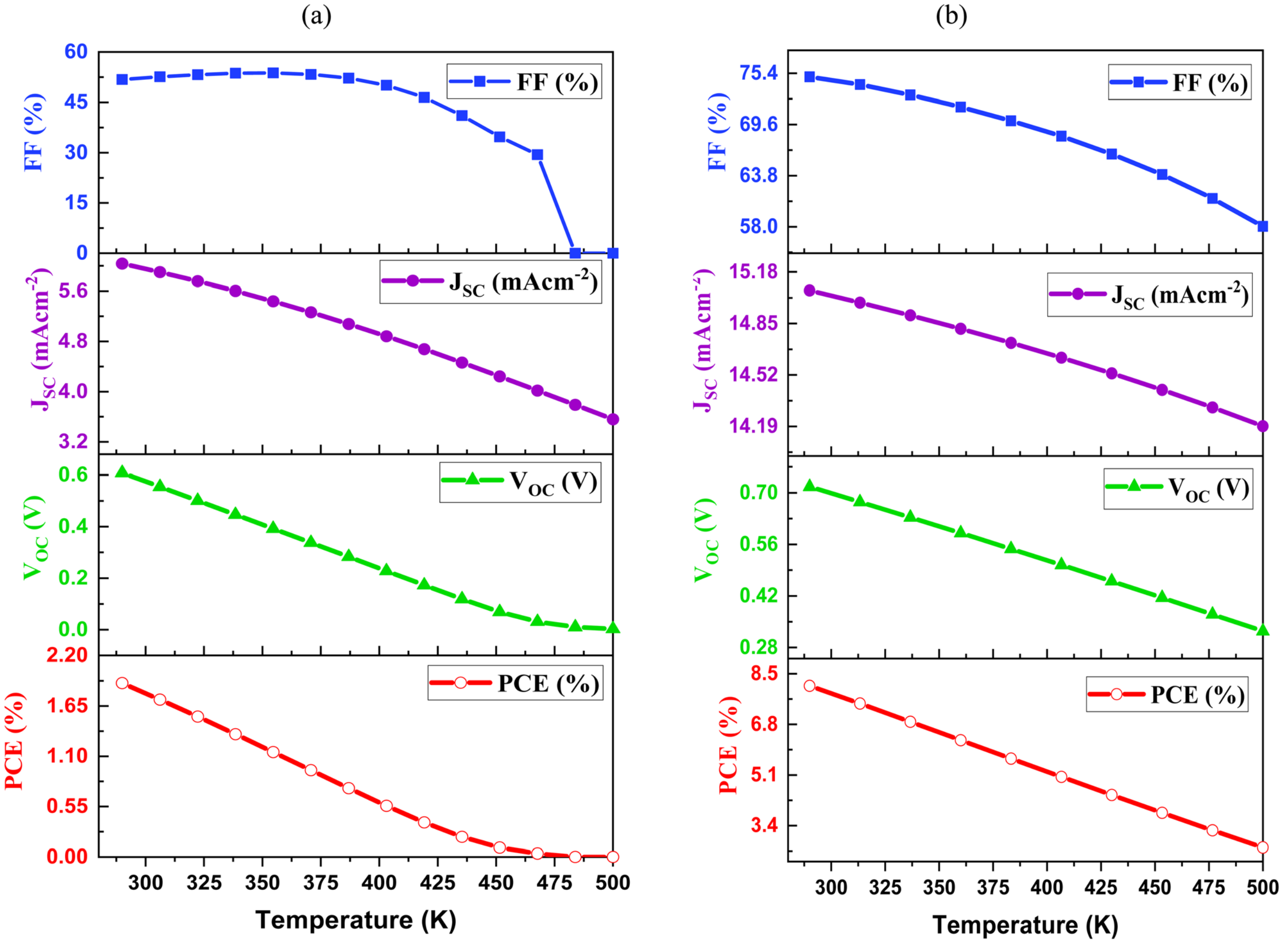

Fig. 8 Impact of working point temperature on the photovoltaic performance of (a) P3HT/N2200 bilayer and (b) P3HT:N2200 bulk heterojunction structured photovoltaic devices.

cm^{-3} both for N_D type and N_A type doping densities shown in Fig. 9(a), (b), (c) and (d), respectively. At this low doping range, recombination and transport are dominated by intrinsic properties of the P3HT:N2200 layer. At higher N_D (>10^{14} cm^{-3}), V_{OC} gradually decreases and steadily increases at higher N_A (>10^{14} cm^{-3}) shown in Fig. 9(a). At higher N_A, the material becomes more strongly p-type causing the Fermi level to shift closer towards the valence band. This increases the built-in potential (V_{bi}) of the junction, which in turn enhances the device V_{OC}.[95] However, higher N_D indicates more free electrons that increase the non-radiative recombination resulting in a decrease in V_{OC}.[96] The J_{SC} decays rapidly for $N_A > 10^{14}$ cm^{-3} due to higher N_A concentration, which increases non-radiative recombination, particularly Auger recombination that reduces the number of charge carriers available for current generation,[97] shown in Fig. 9(b). Also, J_{SC} shows its highest value 15.46 mA cm^{-2} at $N_D = 10^{16}$ cm^{-3} and then decreases slowly as for N_D at higher donor concentration (N_D). The FF of the device initially declines sharply from $N_A = 10^{14}$ to 10^{16} cm^{-3} reaching a minimum value ~47% due to dominant trap-assisted recombination. It has also been observed that the FF dramatically increases at higher acceptor doping (N_A), which is shown in Fig. 9(c). This sudden improvement in the FF can be attributed to the increase in V_{OC} at a higher doping level shown in Fig. 9(a), which reduces resistive losses and results in more efficient charge extraction at this doping level. However, the FF remains stable at low N_D type doping, experiences a slight increase under moderate doping due to improved charge transport and then very slowly decreases because of trap-assisted recombination at higher N_D.[98]

For N_D, the power conversion efficiency of the device peaks around 7.8% at a low doping level (≤10^{14} cm^{-3}) and then increases to 8.27% maximum PCE at 10^{16} cm^{-3} due to improved J_{SC} and FF of the device shown in Fig. 9(b) and (c), resulting from reduced recombination losses at this moderate doping levels. Ultimately, the PCE collapses at higher doping levels because both J_{SC} and FF of the device decrease at a higher doping level due to increased recombination. Similarly, as the doping level (N_A) increases from 10^{14} cm^{-3} to 10^{16} cm^{-3}, the device PCE decreases, reaching a minimum value of 4.99%. This performance loss arises from the increased recombination and transport limitations induced by excessive acceptor doping in this range, which reduce both J_{SC} and FF of the device. When the N_A density exceeds 10^{16} cm^{-3}, the device PCE again

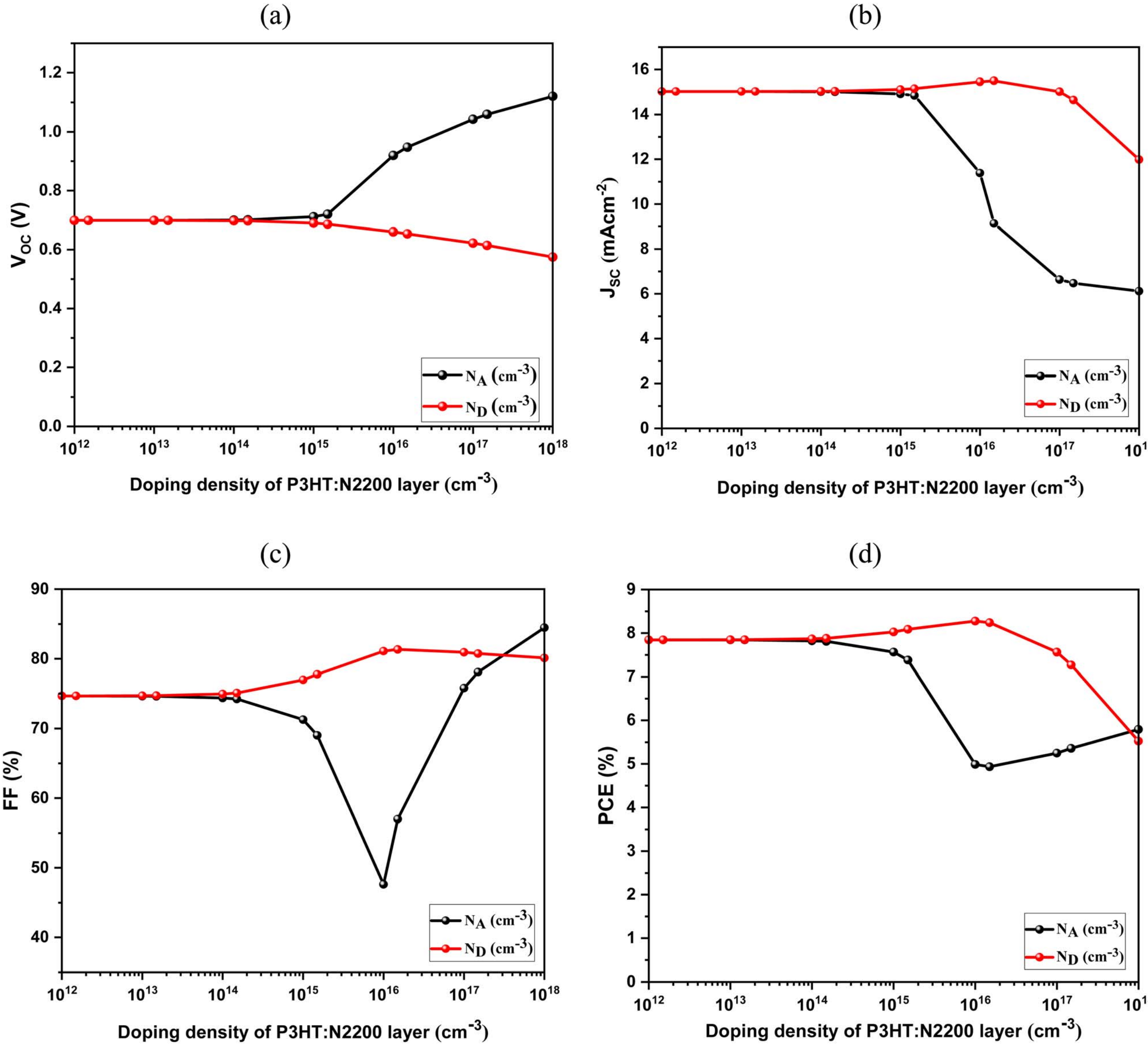

Fig. 9 Impact of the doping density of the P3HT:N2200 active layer on the photovoltaic performance: (a) V_{OC}, (b) J_{SC}, (c) FF, and (d) PCE of the P3HT:N2200 bulk heterojunction structured photovoltaic device.

increases due to the increase in the FF within this range shown in Fig. 9(a). Therefore, an optimum acceptor and donor doping concentration of the P3HT:N2200 active layer was determined at $N_D = 10^{16}$ cm^{-3} and $N_A < 10^{14}$ cm^{-3}, respectively. Here, higher doping densities negatively impact the device PCE because of the space charge effects, which redistribute the internal electric field, leading to decreased charge carrier transport efficiency, increased recombination rates, and ultimately reduced device performance.[99] At low to moderate doping densities both concentrations are sufficient for efficient charge transport and balanced carrier generation, which lead to stable device efficiency. Therefore, an optimal doping density (10^{16} to 10^{17} cm^{-3}) is required to maintain balanced carrier transport and overall device PCE maximization.

3.7. Impact of the bandgap and bulk defect density of the P3HT:N2200 active layer on the photovoltaic device performance

Contour mapping of the photovoltaic performance with respect to the thickness (100 nm to 1000 nm) and bandgap (1.4 eV to 1.8 eV) variation of the P3HT:N2200 layer is shown in Fig. 10. The greatest V_{OC} of the device is observed at higher thickness (750 to 1000 nm) and within the 1.4 eV to 1.56 eV bandgap limit of the P3HT:N2200 layer, shown in Fig. 10(a). From Fig. 10(b), it can be observed that the J_{SC} remains higher at a bandgap less than 1.45 eV within the thickness from 300 nm to 8000 nm of the P3HT:N2200 layer. A similar trend has also been observed for the PCE of the device shown in Fig. 10(d). This indicates that both the J_{SC} and PCE values improve in this bandgap and thickness range. This improvement in PCE and J_{SC} is attributed

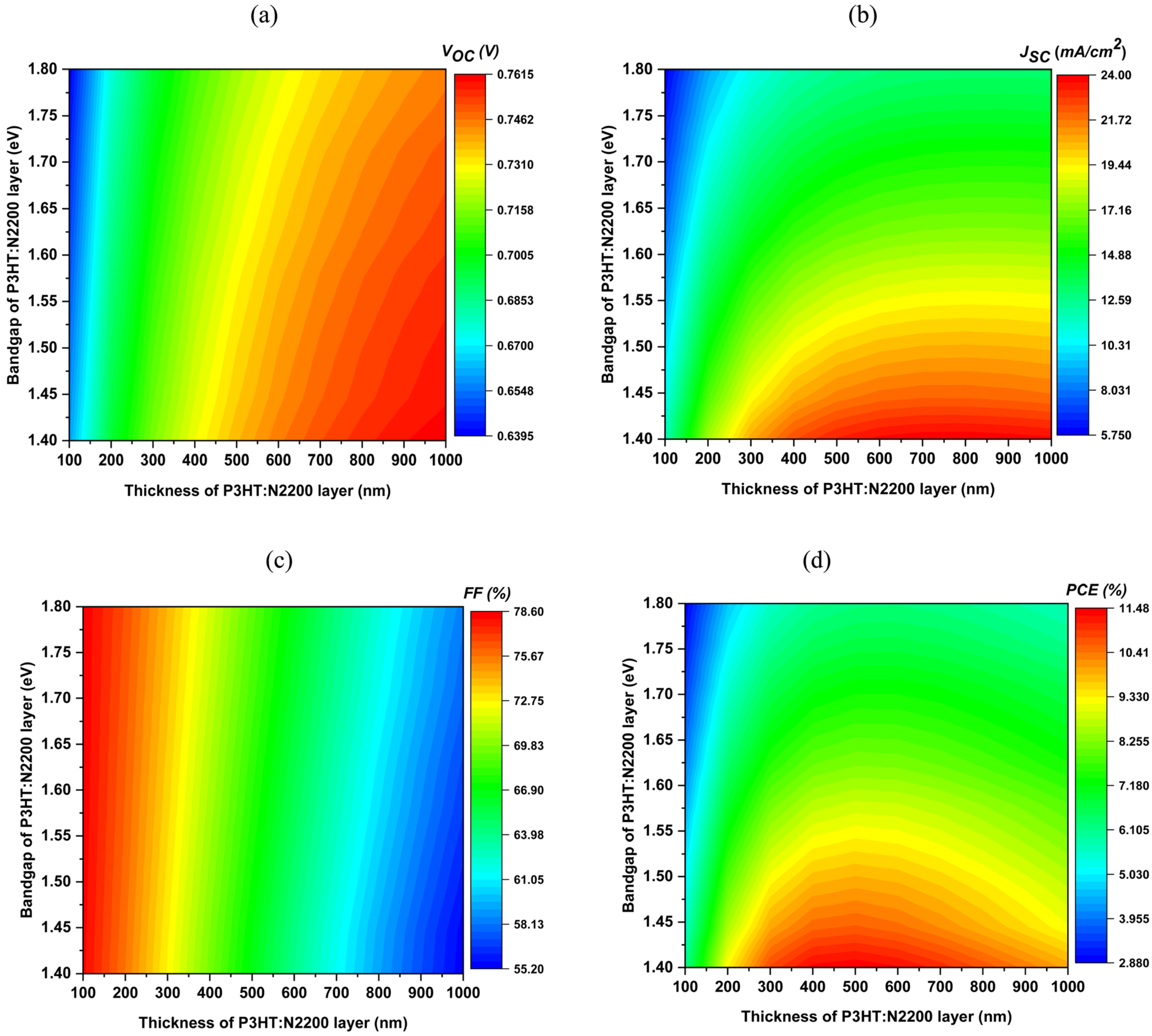

Fig. 10 Contour mapping of photovoltaic performance: (a) V_{OC}, (b) J_{SC}, (c) FF, and (d) PCE of the bulk heterojunction structured photovoltaic device with respect to the thickness and bandgap of the P3HT:N2200 layer.

to the enhanced photon absorption in the thicker active layer, which generates a large number of electron–hole pairs.[100] However, the device FF decreases with increasing thickness of the active layer, which is shown in Fig. 10(c). This can be attributed to the enhanced series resistance and poor charge carrier collection within the thick P3HT:N2200 layer.[100] To maximize the PCE of the device, a thick layer and a bandgap <1.45 eV of the P3HT:N2200 layer balance the absorption and effective carrier collection. Therefore, the optimum bandgap of the P3HT:N2200 layer is 1.40 eV for higher device PCE. A lower bandgap of the active layer enhances compatibility with the solar spectrum, which improves device PCE significantly.[101] This variation to 1.4 eV was part of a standard sensitivity analysis to explore general design principles. Therefore, in our simulation work it does not imply that the P3HT:N2200 material changes. Instead, it theoretically demonstrates the performance benefit that could be gained from a future, lower-bandgap blend with similar transport properties, providing guidance for new material development. This may benefit the pursuit of lower-bandgap polymer acceptors or donor–acceptor pairs while maintaining good charge transport.

3.8. Impact of thickness and bulk defect density of the P3HT:N2200 active layer on the photovoltaic device performance

The thickness and defect density of the active layer significantly influence the performance of photovoltaic devices. Research indicates that an optimal thickness enhances light absorption and reduces recombination losses, while lower defect densities improve charge carrier efficiency.[102,103] The interplay between these factors is crucial for maximizing the device PCE. In

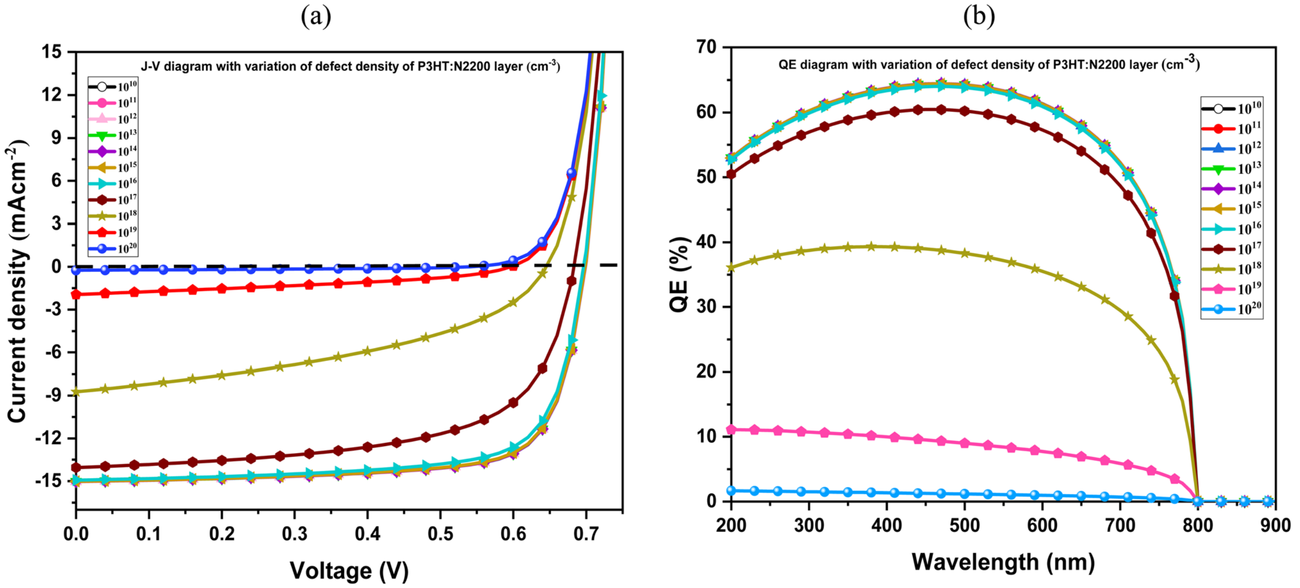

Fig. 11 (a) J–V characteristics and (b) QE spectra of the bulk heterojunction structured photovoltaic device with respect to the thickness and total defect density of the P3HT:N2200 layer.

Fig. 11(a) and (b), the J–V characteristics and QE spectra have been displayed with respect to the change in the total bulk defect density in the P3HT:N2200 active layer. Fig. 11(a) indicates that a lower defect density in the absorber is beneficial for better device performance due to efficient charge carrier collection, whereas excessive defect density enhances carrier recombination, which reduces the effective electric field within the device[104] Similarly, at lower defect densities in the active layer, QE spectra remain high peaking above 60% to 64% in the visible region shown in Fig. 11(b), which confirmed the excellent charge carrier collection and minimum recombination. So, the optimum defect density for the P3HT:N2200 solar cell is around 1×10^{10} cm^{-3} to 1×10^{12} cm^{-3}. Contour mapping of the photovoltaic performance with respect to the thickness (100 nm to 1000 nm) and bulk defect density (1×10^{10} cm^{-3} to 1×10^{20} cm^{-3}) of the P3HT:N2200 layer is shown in Fig. 12. The greatest V_{OC} of the device has been observed at higher thickness (750 nm to 1000 nm) and within the 1×10^{10} cm^{-3} to 1×10^{15} cm^{-3} defect density limit of the P3HT:N2200 layer shown in Fig. 12(a). From Fig. 12(b), it can be observed that the J_{SC} increases at 1×10^{10} cm^{-3} to 1×10^{16} cm^{-3} defect density and 400 nm to 1000 nm thickness of the P3HT:N2200 layer. A similar trend has also been observed for the PCE of the device, as shown in Fig. 12(d). From the J–V characteristics and contour graphs, it clearly indicates that the degradation in photovoltaic metrics arises from the enhanced defect density of the P3HT:N2200 layer. This is because higher defect densities lower the carrier life time and also their diffusion lengths, which are responsible for surface recombination pathways, thereby diminishing the photovoltaic parameters.[77] Therefore, the results suggest that well defined thickness of the P3HT:N2200 active layer with low bulk defect densities is the key to achieve better photovoltaic performance.

3.9. Impact of bulk defect density in the P3HT:N2200 layer with the interfacial defect densities at PEDOT:PSS/P3HT:N2200 and P3HT:N2200/BCP junctions on the device performance

The photovoltaic performance is strongly influenced by the defect levels of the active layer and by the defects present at the interfaces. Shubham *et al.* reported that interfacial defect optimization is crucial for an efficient device.[105] The photovoltaic performance is strongly influenced by interfacial recombination, as recombination at the junction between the active layer and the transport layers leads to the formation of interface defect states.[106] Contour mapping of the photovoltaic performance with respect to the bulk defects in the P3HT:N2200 layer (1×10^{12} cm^{-3} to 1×10^{18} cm^{-3}), with the interfacial defect densities at PEDOT:PSS/P3HT:N2200 and P3HT:N2200/BCP junctions (1×10^{7} cm^{-2} to 1×10^{16} cm^{-2}), is shown in Fig. 13(a–h). The overall device efficiency decreased at high defects, as both the bulk and interfacial defect densities increased, as shown in Fig. 13(d). This is because the increased defects lead to more trap levels present at the interface, reducing device efficiency.[107] It is evident that higher defect states both for P3HT:N2200 and PEDPT:PSS/P3HT:N2200 interfaces deteriorate the overall photovoltaic metrics (V_{OC}, J_{SC}, FF & PCE), as shown in Fig. 13(a–d). The increased interfacial defects lead to higher charge recombination which accelerates carrier loss at the interface.[108,109] This results in reduced charge carrier lifetime and collection efficiency which in turn causes a substantial degradation of the key photovoltaic parameters and overall device performance. In contrast, the photovoltaic device parameters are independent of the P3HT:N2200/BCP interface defect density, shown in Fig. 13(e–h). Here, the P3HT:N2200/ETL defect density does not significantly affect the device performance. This can be attributed to the lower photogenerated charge carrier density as the

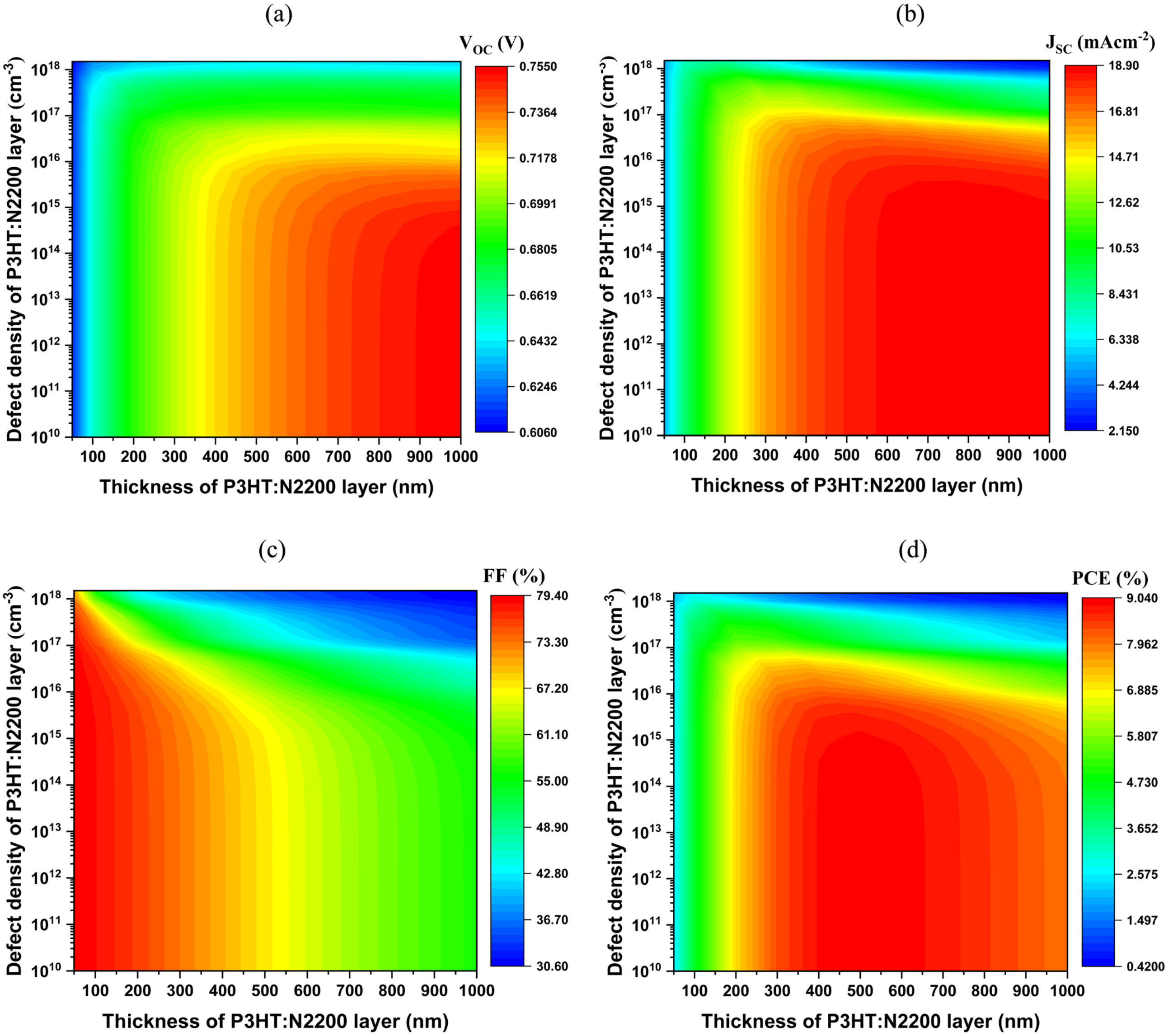

Fig. 12 Contour mapping of photovoltaic performance: (a) V_{OC}, (b) J_{SC}, (c) FF, and (d) PCE of the bulk heterojunction structured photovoltaic device with respect to the thickness and total defect density of the P3HT:N2200 layer.

illumination occurred through the PEDOT:PSS or HTL layer rather than the BCP or ETL layer.[107] Also, the ETL side may not be the dominant recombination pathway as most of the recombination happens inside the active layer (P3HT:N2200) and HTL/P3HT:N2200 interface. Therefore, optimization of the interface defect density at the PEDOT:PSS/P3HT:N2200 interface layer is very crucial for achieving high performance photovoltaic device fabrication in this configuration.

3.10. Impact of electron affinity and dielectric permittivity of the P3HT:N2200 active layer on the device performance

The electron affinity and dielectric permittivity of the P3HT:N2200 layer play a vital role in the photovoltaic performance. A suitable choice of electron affinity ensures proper energy level alignment between the P3HT donor and N2200 acceptor materials. This proper alignment facilitates efficient exciton generation, dissociation and charge carrier transport. Also, the dielectric permittivity strongly impacts the strength of the Coulomb interaction during exciton formation, which also impacts efficient charge carrier separation and recombination rates. Leblebici *et al.* reported that an absorber material with suitable electron affinity and dielectric permittivity is crucial for improving device efficiency of organic solar cells.[110] Therefore, the electron affinity and dielectric permittivity optimization of the P3HT:N2200 layer is essential for an efficient photovoltaic device. Fig. 14(a) and (b) display how the variation of electron affinity (3.0 eV to 4.0 eV) and Fig. 14(c) and (d) present how the variation of dielectric permittivity (3 eV to 5.0 eV) of the P3HT:N2200 layer depend on the photovoltaic parameters. The short circuit current density (J_{SC}) remains constant across this electron affinity range, indicating that the photogenerated current does not significantly affect as electron affinity mainly

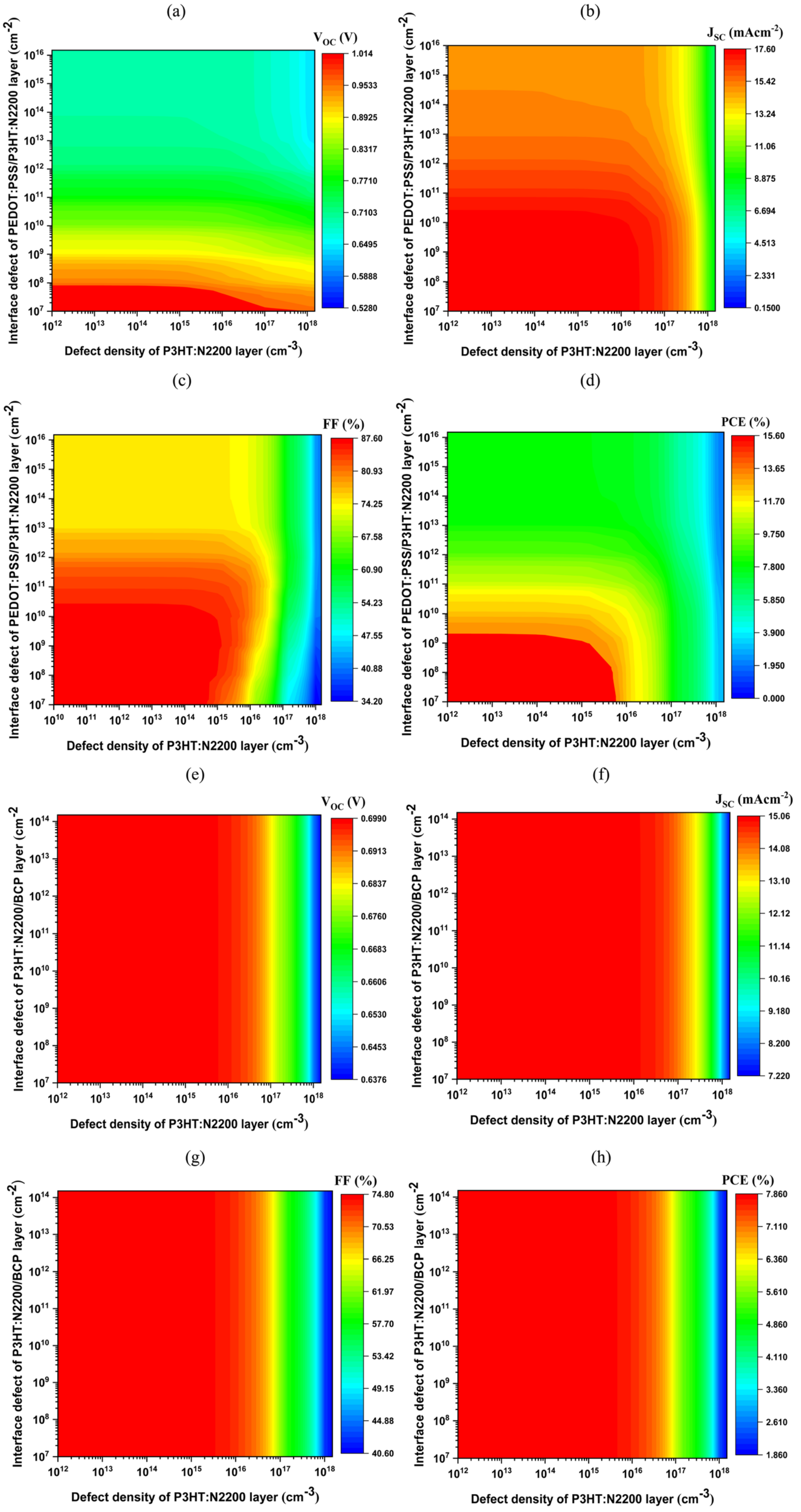

Fig. 13 Contour mapping of photovoltaic performance parameters of the bulk heterojunction structured photovoltaic device as a function of bulk defect density in the P3HT:N2200 layer with the interfacial defect densities at ((a)–(d)) PEDOT:PSS/P3HT:N2200 and ((e)–(h)) P3HT:N2200/BCP junctions.

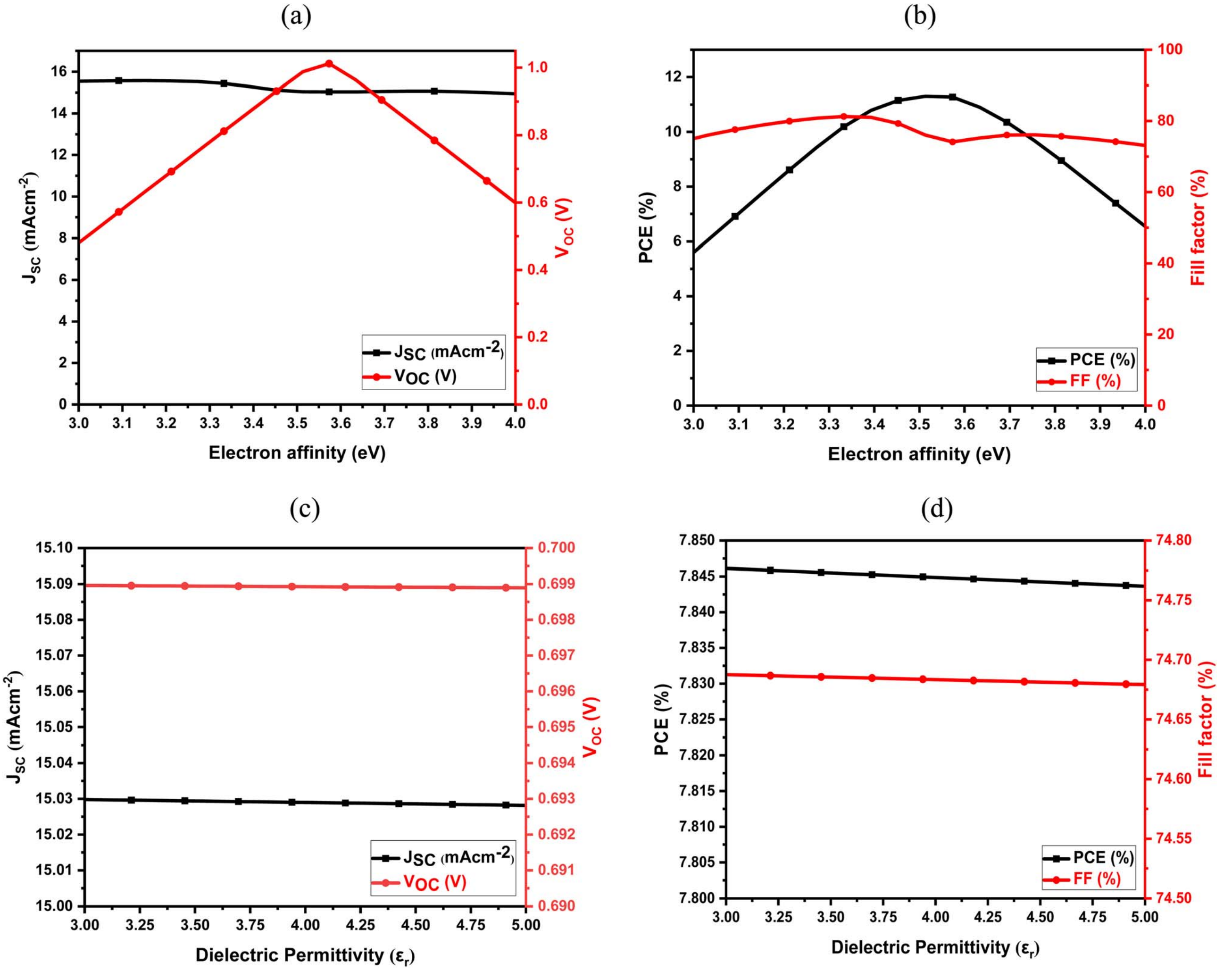

Fig. 14 Impact of (a) & (b) electron affinity and (c) & (d) dielectric permittivity variation of the P3HT:N2200 layer on the device performance.

shifts energy levels (which affect V_{OC}) rather than the number of carriers that are generated and extracted.[111] It has been observed that the V_{OC} initially increases from 0.5 V to a maximum of 1.01 V (with a peak value at 3.57 eV) with increased electron affinity due to proper energy level alignment, which reduces recombination. Beyond this 3.57 eV the V_{OC} starts to decline because of unfavorable energy band alignment of the P3HT with the N2200 levels, which leads to diminished charge separation efficiency, thus lowering V_{OC}.[112] The FF is also not significantly affected by variations in electron affinity. An identical behavior to that of V_{OC} has been observed for PCE. The highest PCE of 11.33% was achieved when the electron affinity was set at approximately 3.53 eV, shown in Fig. 14(b). The observed variation in PCE arises from the combined influence of V_{OC}, J_{SC} and FF. This emphasizes the significance of an optimum value of electron affinity to achieve optimal device performance.

In contrast, the dielectric permittivity variation of P3HT:N2200 within this range does not have a major effect on the photovoltaic parameters shown in Fig. 14(c) and (d). However, dielectric permittivity is an important factor for the design of the active layer, and its variation within this range does not significantly affect the photovoltaic parameters. Moreover, the literature demonstrates that an increased dielectric permittivity improves the junction's capability to separate charge carriers, lowering recombination rates and enabling more efficient current extraction.[113]

3.11. Impact of electron and hole mobility of the P3HT:N2200 active layer on the device performance

The effect of electron and hole mobility of the P3HT:N2200 layer on the photovoltaic parameters is shown in Fig. 15 within the range of 1×10^{-5} cm^2 V^{-1} s^{-1} to 10 cm^2 V^{-1} s^{-1}. The V_{OC} of the device increases with higher hole mobility due to improved hole extraction whereas, it decreases when the electron mobility becomes higher, as shown in Fig. 15(a). Here, the higher electron mobility creates a mobility imbalance and enhances recombination, leading to a reduction in device V_{OC}.[114] It has been observed that the J_{SC} of the device increases at higher electron and hole mobilities shown in Fig. 15(b). This is because higher mobility also enhances the material's conductivity which in turn reduces

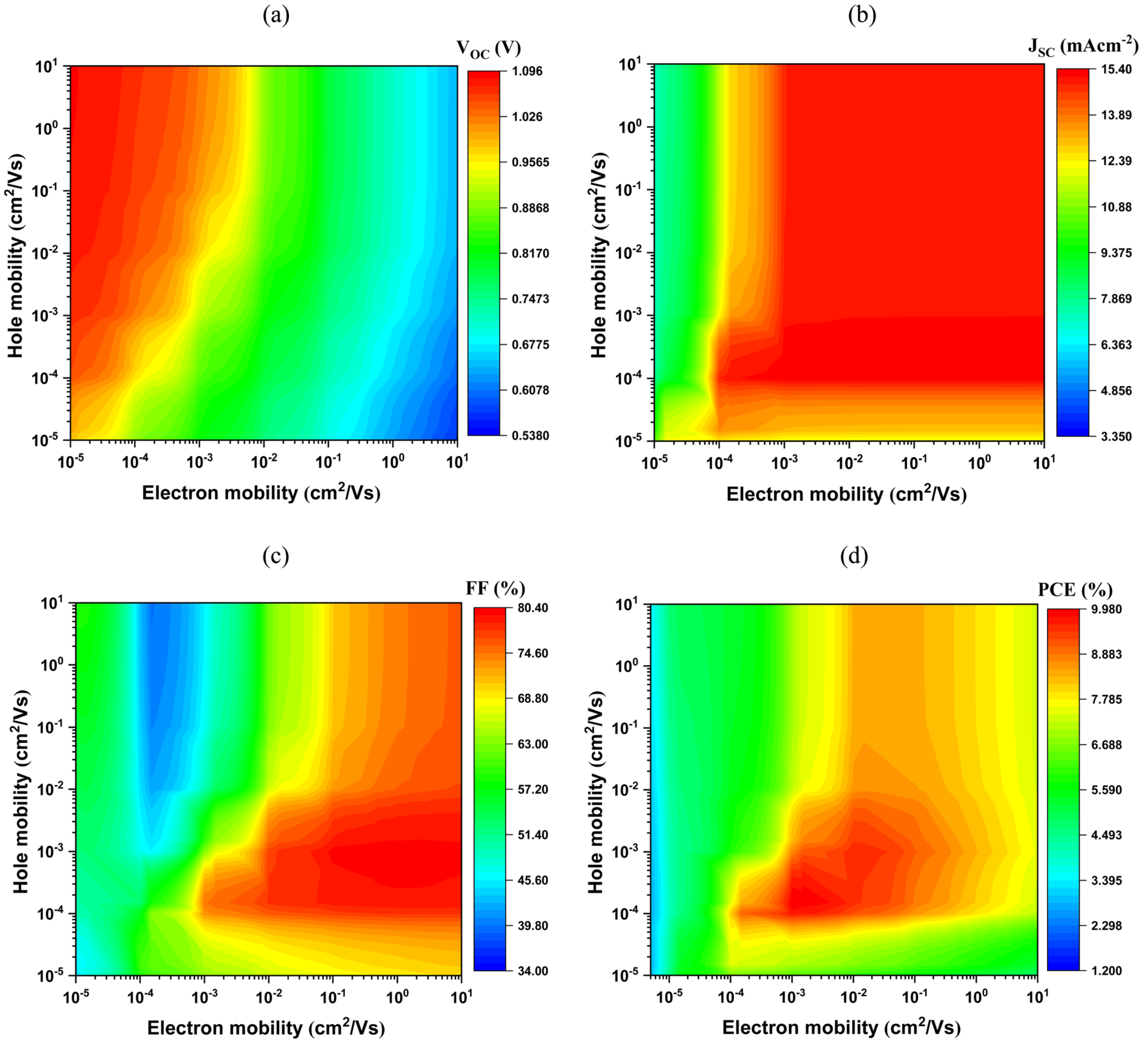

Fig. 15 Contour mapping of photovoltaic performance parameters: (a) V_{OC}, (b) J_{SC}, (c) FF, and (d) PCE of the bulk heterojunction structured photovoltaic device as a function of electron and hole mobility in the P3HT:N2200 layer.

the series resistance. From Fig. 15(c), it can be said that a higher FF occurs when the mobilities are balanced and moderately high. Balanced carrier mobility minimizes space-charge buildup and reduces recombination, leading to efficient charge extraction which maximizes the FF. Similarly, the power conversion efficiency of the device reached its maximum value at an electron mobility from 1×10^{-3} cm^2 V^{-1} s^{-1} to 1×10^{-2} cm^2 V^{-1} s^{-1} and hole mobility from 1×10^{-4} cm^2 V^{-1} s^{-1} to 1×10^{-3} cm^2 V^{-1} s^{-1}. This is an optimal range of carriers mobilities, where both extraction and recombination losses are minimized, thereby maximizing the device PCE.[115] Similar simulation results were reported by Aaqik *et al.* using a P3HT:PCBM based organic solar cell by varying the electron and hole mobilities of the P3HT buffer layer.[34] Nojima *et al.* reported that the carrier mobility in the order of 1×10^{-4} cm^2 V^{-1} s^{-1} for electrons and holes shows the best device PCE using P3HT and PCBM materials.[116] Therefore, balanced electron and hole mobility is essential for achieving an efficient photovoltaic device.

3.12. Impact of series (R_S) and shunt (R_{SH}) resistance on the device performance

Photovoltaic performance is strongly influenced not only by the intrinsic properties of the active layer but also by the electrical characteristics of the device such as series resistance and shunt resistance. Series resistance arises from the connections and junctions formed by layers (P3HT:N2200, HTL, ETL, *etc.*) and electrodes whereas, shunt resistance represents leakage pathways in the device caused by pinholes, defects or imperfect interfaces.[117] Fig. 16 illustrates the effect of series and shunt resistance on the photovoltaic parameters within the ranges of 0 Ω cm^2 to 10 Ω cm^2 and 0 Ω cm^2 to 1000 Ω cm^2, respectively. The subsequent evaluation of V_{OC}, J_{SC}, FF and PCE of the device

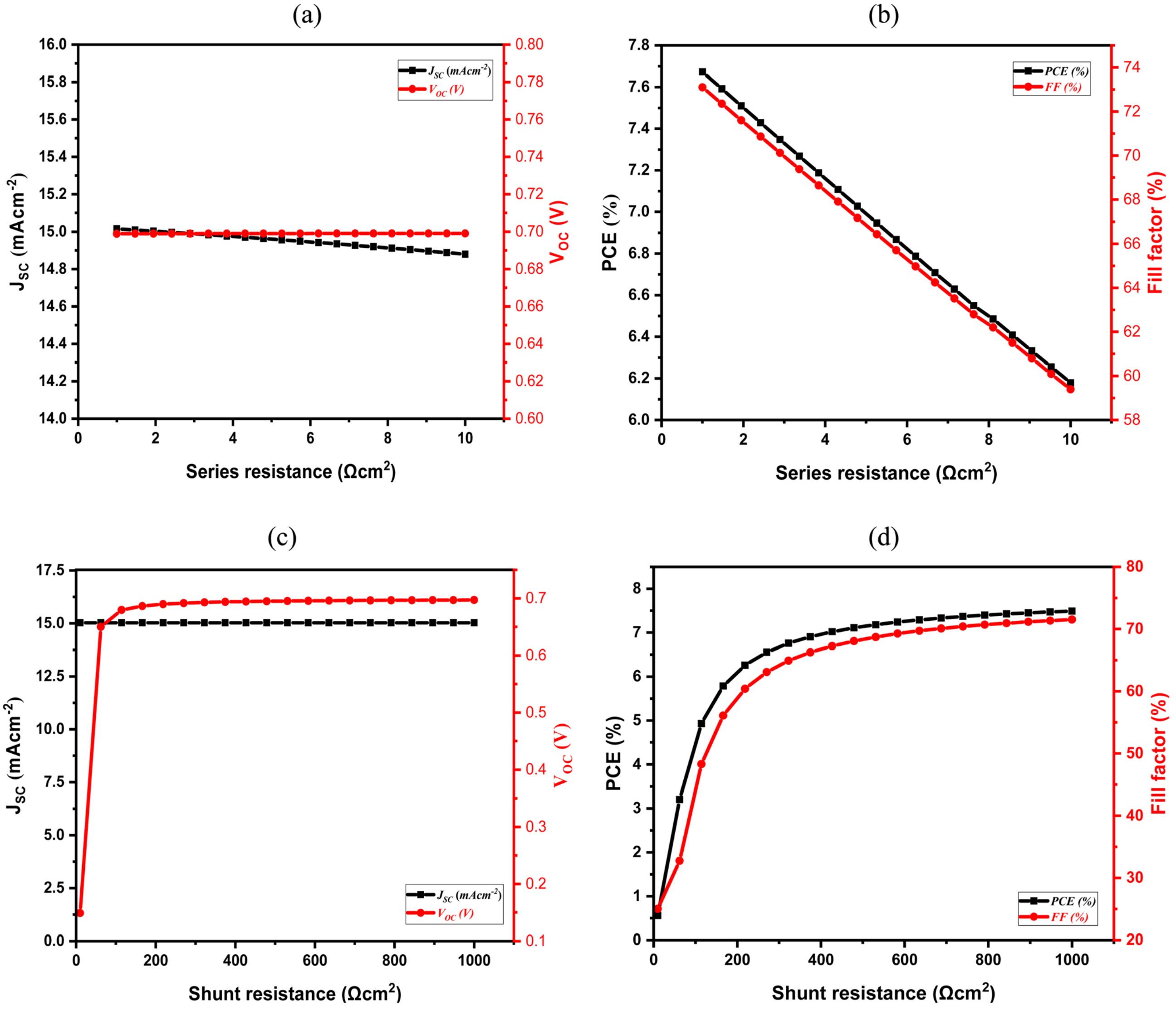

Fig. 16 Impact of (a) & (b) series resistance and (c) & (d) shunt resistance variation of the P3HT:N2200 layer on the device performance.

is shown in Fig. 16(a) and (b) for R_S and 16(c) and (d) for R_{SH}. No significant changes in the device J_{SC} are observed with the variations in R_S and R_{SH} as shown in Fig. 16(a) and (c), respectively. Also, the device V_{OC} remains almost unaffected by the variation in R_S. However, in the case of R_{SH}, V_{OC} increases sharply from 10 Ω cm^2 to 62 Ω cm^2 followed by a gradual rise up to 270 Ω cm^2 and then becomes saturated. However, the FF and PCE are significantly impacted by the variation of both R_S and R_{SH}. A degradation in the FF and PCE of the device has been observed with increasing R_S, shown in Fig. 16(b). When the device R_S increases from 1 Ω cm^2 to 10 Ω cm^2, the PCE drops from 7.67% to 6.18%, indicating a 19.4% relative loss in PCE. This is because an increase in series resistance leads to higher resistive losses and impedes charge transport, resulting in a reduction of the device PCE.[118] However, the device FF and PCE improve significantly as the R_{SH} increases from 10 Ω cm^2 to 1000 Ω cm^2. At very low R_{SH}, poor PCE has been observed because of severe current leakage through shunting pathways. However, this leakage current is suppressed at a higher R_{SH} value. This is because the current leakage paths are minimized at higher R_{SH}, which ensures efficient charge carrier transport leading to an improved device PCE.[92] The power conversion efficiency and fill factor of the device experience a nonlinear response at higher R_{SH}, which is observed in Fig. 16(d), where the FF reaches around 71.5% and PCE stabilizes at about 7.49%. Therefore, shunt path minimization is very crucial for efficient device fabrication.[119]

3.13. Optimized device performance

Fig. 17 presents the comparative analysis of photovoltaic performance of the device simulated with the initial set of parameters and the optimized set of parameters of the P3HT:N2200 layer. The optimized values are listed in Table 2. It has been observed that the optimized device leads to a significant enhancement in the photovoltaic metrics shown in Table 3. The J–V characteristics of the initial structure before

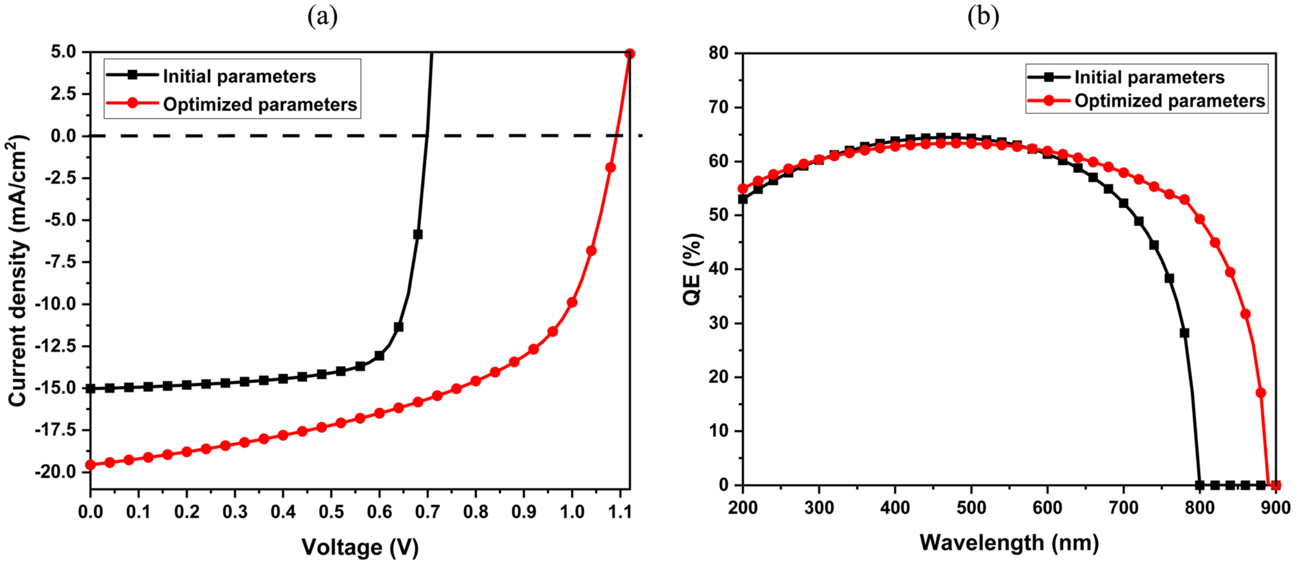

Fig. 17 (a) Current density–voltage (J–V) characteristics after illumination; (b) QE spectrum of P3HT:N2200 bulk heterojunction photovoltaic device simulated with initial (black line) and optimized parameters (red line) of the P3HT:N2200 layer.

Table 2 The optimized values of the P3HT:N2200 layer

Optimized parameter	Optimized value
Thickness (nm)	500
Band gap (eV)	1.4
Electron affinity (eV)	3.53
Electron mobility (cm^2 V^{-1} s^{-1})	1×10^{-2}
Hole mobility (cm^2 V^{-1} s^{-1})	1×10^{-3}
Shallow uniform donor density (cm^{-3})	1×10^{16}
Shallow uniform acceptor density (cm^{-3})	1×10^{14}

optimization notably change after the optimization, which is displayed in Fig. 17(b). The V_{OC} increased from 0.699 V to 1.092 V due to improved energy level alignment at the interfaces after the optimization of the parameters. This reduces recombination losses resulting in a higher built-in potential, which in turn increases V_{OC}. J_{SC} increased from 15.029 mA cm^{-2} to 19.573 mA cm^{-2} due to enhanced light absorption and more efficient carrier extraction at the electrodes, as confirmed by the improvement in the QE spectra. However, the FF declined from 74.684% to 55.371%, resulting from the higher internal losses in the optimized structure arising from the higher series resistance. Finally, the device PCE increased from 7.845% to 11.834% despite the reduction in the FF. The significant increment in both V_{OC} and J_{SC} more than compensates, leading to a higher overall PCE. The combined effect of improved charge separation, efficient charge collection and optimized energy level alignment contributes to this efficiency enhancement.

Table 3 Photovoltaic parameters of the devices using initial parameters and optimized parameters

Photovoltaic parameter	Initial device	Optimized device
V_{OC} (V)	0.699	1.092
J_{SC} (mA cm^{-2})	15.029	19.573
FF (%)	74.684	55.371
PCE (%)	7.845	11.834

A broader QE spectrum than the initial QE is shown in Fig. 17(b). The QE of the optimized device follows the similar profile up to around 600 nm wavelength, indicating that the photon absorption at shorter wavelengths remains unchanged after the optimization. Initially the QE spectrum drops to zero at 800 nm but the bandgap optimization of the P3HT:N2200 layer extends the spectral response of the optimized device up to 900 nm, suggesting improved light absorption at longer wavelengths. However, the additional optimizations of thickness, defect density, and other parameters improve the device performance metrics like V_{OC}, J_{SC} and PCE. This enhancement in the QE and device PCE can be attributed to the optimized parameters of the P3HT:N2200 active layer, which improved the absorption of low-energy photons, efficient carrier transport and extraction within the P3HT:N2200 active layer.

3.14. Comparison of simulation and experimental results

In Table 4, the power conversion efficiency obtained from this simulation is compared with previously reported experimental results only, as no simulation studies on the P3HT:N2200 BHJ system have been reported to date using SCAPS-1D simulation. The experimentally reported PCE for the P3HT:N2200 BHJ device is 0.17% (ref. 45), which improves to 0.21% after annealing the blend film. The most significant enhancement in PCE reaching 0.65% was reported when combining 1% DIO and annealing treatment of the BHJ film at a thickness ∼100 nm. In another experimental report, the PCE of the P3HT:N2200 blend was reported to be 0.82%, which was substantially enhanced to 1.4% by incorporating near IR sensitizers such as SiNc10 at

Table 4 Comparison between simulation and experimental results

Research type	Active layer thickness (nm)	Reported PCE (%)	Processing conditions
Experiment[45]	100	0.17	—
		0.65	1% DIO + annealing
Experiment[46]	110	0.82	—
		1.40	Near-IR sensitizers
Experiment[11]	—	0.10	—
		0.36	DIO + methanol
Experiment[120]	80–110	0.09	—
This simulation	100	4.56	Idealized, defect limited model

a thickness of approximately 100 nm.[46] A recent experimental study on this device showed a relatively low PCE, which improved from 0.10% to 0.36% using DIO and methanol treatment,[11] consistent with the other reported results. However, under the same thickness (100 nm) of P3HT:N2200, this simulation predicts a significantly higher PCE of 4.56%, which is shown in Fig. 7(c). This deviation from the experimental value can be ascribed to the idealized conditions during the SCAPS-1D simulation, such as uniform P3HT:N2200 film morphology, low defects and optimized charge transport parameters, which are very difficult to achieve experimentally during device fabrication. Despite this discrepancy, the simulation results successfully capture the experimental trend observed across these studies.

4. Conclusion

This work initially conducted a comparative simulation study of bilayer and BHJ organic solar cell devices using the SCAPS-1D tool by incorporating P3HT donor and N2200 acceptor polymers. The simulation results reveal that the BHJ device exhibits superior photovoltaic performance compared to the bilayer device. It has been observed that the BHJ device shows a short circuit current density (J_{SC}) of 15.029 mA cm^{-2}, open circuit voltage (V_{OC}) of 0.699 V, fill factor (FF) of 74.684% and power conversion efficiency (PCE) of 7.845%, whereas the bilayer device exhibits a J_{SC} of 5.952 mA cm^{-2}, V_{OC} of 0.575 V, FF of 52.293% and PCE of 1.79%. The thickness variation studies were conducted for both bilayer and BHJ architectures to find out the optimum thickness of the P3HT, N2200 and P3HT:N2200 layers. In the case of the bilayer device, the combined optimum thickness of the P3HT donor and N2200 acceptor layers was recorded as 35–40 nm and >100 nm, respectively, shown in Fig. 6(c) and (d). Conversely, for the BHJ device, the optimum P3HT:N2200 active layer thickness was recorded as 500 nm. These findings highlight the performance advantage of BHJ structures and provide guidance for thickness optimization in P3HT and N2200-based OPV devices. It has also been concluded that as the temperature increases from 300 K to 500 K, the PCE of both devices decreases due to a higher recombination rate at elevated temperatures.

To improve the overall performance of the BHJ device, the effects of doping density, bandgap variation, bulk and interfacial defects, electron affinity, dielectric permittivity and charge-carrier mobility have been systematically investigated. The simulation results depict that increasing the bandgap of the P3HT:N2200 layer leads to a reduction in device efficiency with a maximum PCE at an effective bandgap of 1.4 eV where an optimal doping density ($N_A \leq 10^{14}$ cm^{-3} and $N_D \sim 10^{16}$ cm^{-3}) is required to maintain balanced carrier transport and overall device PCE maximization. Additionally, minimizing the bulk and interfacial defect states is paramount for achieving better device performance. The electron affinity variation of the P3HT:N2200 layer yields maximum device PCE at 3.53 eV, while changes in dielectric permittivity exhibit no significant influence on the device performance metrics. In addition, the charge-carrier mobility analysis indicates that the device attains its maximum PCE when the electron mobility is between 1×10^{-3} cm^2 V^{-1} s^{-1} and 1×10^{-2} cm^2 V^{-1} s^{-1} and the hole mobility is between 1×10^{-4} cm^2 V^{-1} s^{-1} and 1×10^{-3} cm^2 V^{-1} s^{-1}. Furthermore, the impact of series and shunt resistances was investigated.

The study identified a set of optimum values of the physical and electrical parameters that maximize the photovoltaic device parameters. Incorporating this set of optimized parameters led to a notable improvement in the overall device performance. The optimized OPV device achieved a J_{SC} of 19.573 mA cm^{-2}, V_{OC} of 1.092 V and PCE of 11.834% compared to the initial device configuration.

Conflicts of interest

There are no conflicts to declare.

Data availability

All data are available from the corresponding author upon reasonable request.

Acknowledgements

The authors are thankful to Professor Marc Burgelman, University of Ghent, Belgium, for making the SCAPS simulation software freely available to the photovoltaic research community.

References

1 Y. Li, X. Huang, K. Ding, H. K. M. Sheriff, L. Ye, H. Liu, C. Z. Li, H. Ade and S. R. Forrest, Non-fullerene acceptor

organic photovoltaics with intrinsic operational lifetimes over 30 years, *Nat. Commun.*, 2021, **12**, 5419, DOI: 10.1038/s41467-021-25718-w.

2 W. Liu, J. Yuan, C. Zhu, Q. Wei, S. Liang, H. Zhang, G. Zheng, Y. Hu, L. Meng, F. Gao, Y. Li and Y. Zou, A-π-A structured non-fullerene acceptors for stable organic solar cells with efficiency over 17, *Sci. China:Chem.*, 2022, **65**, 1374–1382, DOI: 10.1007/s11426-022-1281-0.

3 Q. Liu, Y. Jiang, K. Jin, J. Qin, J. Xu, W. Li, J. Xiong, J. Liu, Z. Xiao, K. Sun, S. Yang, X. Zhang and L. Ding, 18% Efficiency organic solar cells, *Sci. Bull.*, 2020, **65**, 272–275, DOI: 10.1016/j.scib.2020.01.001.

4 N. Espinosa, M. Hösel, M. Jørgensen and F. C. Krebs, Large scale deployment of polymer solar cells on land, on sea and in the air, *Energy Environ. Sci.*, 2014, **7**, 855, DOI: 10.1039/c3ee43212b.

5 C. S. Kundu, A. Adhikary, M. S. Ahsan, A. Rahaman, M. B. Hossain, A. D. Raha, S. A. Murad and F. Ahmed, Design and analysis of performance parameters for achieving high efficient ITO/PEDOT:PSS/P3HT:PCBM/Al organic solar cell, *J. Opt.*, 2024, **53**, 342–353, DOI: 10.1007/s12596-023-01230-w.

6 B. Chang, B. H. Jiang, C. P. Chen, K. Chen, B. H. Chen, S. Tan, T. C. Lu, C. S. Tsao, Y. W. Su, S. Da Yang, C. S. Chen and K. H. Wei, Achieving High Efficiency and Stability in Organic Photovoltaics with a Nanometer-Scale Twin p-i-n Structured Active Layer, *ACS Appl. Mater. Interfaces*, 2024, **16**, 41244–41256, DOI: 10.1021/acsami.4c08868.

7 L. de Queiroz Corrêa, B. Hellen de Souza Miranda, G. de Amorim Soares and D. Bagnis, From-lab-to-fab: challenges and vision for sustainable organic electronics—organic photovoltaic case, in *Sustainable Strategies in Organic Electronics*, Elsevier, 2022, pp. 521–560, DOI: 10.1016/B978-0-12-823147-0.00015-X.

8 H. Hoppe and N. S. Sariciftci, Organic solar cells: An overview, *J. Mater. Res.*, 2004, **19**, 1924–1945, DOI: 10.1557/JMR.2004.0252.

9 M. N. Uddin and P. Afrin, Comparative performance analysis of poly (3-hexylthiophene-2, 5-dial) and [6,6]-phenyl-C61 butyric acid methyl ester-based organic solar cells in bulk-heterojunction and bilayer structure using SCAPS, *Optik*, 2024, **302**, 171691, DOI: 10.1016/j.ijleo.2024.171691.

10 H. Zhang, Y. Li, X. Zhang, Y. Zhang and H. Zhou, Role of interface properties in organic solar cells: From substrate engineering to bulk-heterojunction interfacial morphology, *Mater. Chem. Front.*, 2020, **4**, 2863–2888, DOI: 10.1039/d0qm00398k.

11 Md. N. Uddin, S. Karmakar, S. Khanam and N. Chawdhury, Investigation of photovoltaic properties of poly(3-hexylthiophene):Polynaphthalene-bithiophene heterostructure devices, *Opt. Mater.*, 2024, **157**, 116385, DOI: 10.1016/j.optmat.2024.116385.

12 A. Mubarik, F. Shafiq and X.-H. Ju, Rational design and DFT-based study of non-fullerene acceptors for high-performance organic solar cells: End-cap and Core modifications for enhanced charge transfer, *Comput. Theor. Chem.*, 2025, **1248**, 115209, DOI: 10.1016/j.comptc.2025.115209.

13 M. N. Uddin, R. Islam, M. Rahman and N. Chawdhury, Comparative Photovoltaics of P3HT:N2200 and P3HT: Small-Gap Fullerene Ethyl-Nipecotate Bulk Heterojunction Structures, *Makara J. Sci.*, 2022, **26**(6), DOI: 10.7454/mss.v26i3.1370.

14 M. Muzammil, K. Naik Naam, M. Fareed, S. H. Mirza and M. Zulfiqar, Boosting the performance of PBDB-T/ITIC based organic solar cell: A theoretical analysis utilizing SCAPS-1D: Boosting the performance of PBDB-T/ITIC based organic solar cell, *Chem. Phys. Impact*, 2024, **8**, 100407, DOI: 10.1016/j.chphi.2023.100407.

15 J. Yuan, Y. Zhang, L. Zhou, G. Zhang, H. L. Yip, T. K. Lau, X. Lu, C. Zhu, H. Peng, P. A. Johnson, M. Leclerc, Y. Cao, J. Ulanski, Y. Li and Y. Zou, Single-Junction Organic Solar Cell with over 15% Efficiency Using Fused-Ring Acceptor with Electron-Deficient Core, *Joule*, 2019, **3**, 1140–1151, DOI: 10.1016/j.joule.2019.01.004.

16 S. Griggs, A. Marks, H. Bristow and I. McCulloch, n-Type organic semiconducting polymers: stability limitations, design considerations and applications, *J. Mater. Chem. C*, 2021, **9**, 8099–8128, DOI: 10.1039/d1tc02048j.

17 Y. Min, C. Dou, D. Liu, H. Dong and J. Liu, Quadruply B-N-Fused Dibenzo-azaacene with High Electron Affinity and High Electron Mobility, *J. Am. Chem. Soc.*, 2019, **141**, 17015–17021, DOI: 10.1021/jacs.9b09640.

18 Y. Li, P. Sonar, L. Murphy and W. Hong, High mobility diketopyrrolopyrrole (DPP)-based organic semiconductor materials for organic thin film transistors and photovoltaics, *Energy Environ. Sci.*, 2013, **6**, 1684–1710, DOI: 10.1039/c3ee00015j.

19 A. Facchetti, Semiconductors for organic transistors, *Mater. Today*, 2007, **10**, 28–37, DOI: 10.1016/S1369-7021(07)70017-2.

20 X. Xu, G. Zhang, L. Yu, R. Li and Q. Peng, P3HT-Based Polymer Solar Cells with 8.25% Efficiency Enabled by a Matched Molecular Acceptor and Smart Green-Solvent Processing Technology, *Adv. Mater.*, 2019, **31**, 1906045, DOI: 10.1002/adma.201906045.

21 C. Yang, S. Zhang, J. Ren, M. Gao, P. Bi, L. Ye, J. Hou, S. Zhang, L. Ye and J. Hou, Molecular design of a non-fullerene acceptor enables a P3HT -based organic solar cell with 9.46% efficiency, *Energy Environ. Sci.*, 2020, **13**, 2864–2869, DOI: 10.1039/d0ee01763a.

22 S. Chatterjee, S. Jinnai and Y. Ie, Nonfullerene acceptors for P3HT-based organic solar cells, *J. Mater. Chem. A*, 2021, **9**, 18857–18886, DOI: 10.1039/d1ta03219d.

23 Y. Min Nam, J. Huh and W. Ho Jo, Optimization of thickness and morphology of active layer for high performance of bulk-heterojunction organic solar cells, *Sol. Energy Mater. Sol. Cells*, 2010, **94**, 1118–1124, DOI: 10.1016/j.solmat.2010.02.041.

24 N. Zhang, Z. Xu, Q. Tang, G. Hu, D. Liu, X. Wang, J. Huang, Q. Zhang, X. Xu, Y. Hu, Y. Peng, S. Xu, L. Sun, W. Lv, L. Jiang, Q. Li and F. Lu, Thickness-ratio-dependent

performances of broadband organic photodiodes based on a tin phthalocyanine/PTCDA heterojunction, *Opt. Lett.*, 2023, **48**, 3579–3582, DOI: 10.1364/ol.488657.

25 A. Bakour, M. Al-Hattab, O. Bajjou and K. Rahmani, Efficiency enhancement of novel ITO/ZnSe/CNTs thin film solar cell, *Chem. Phys. Impact*, 2024, **9**, 100672, DOI: 10.1016/j.chphi.2024.100672.

26 W. Zein, T. I. Alanazi, A. Saeed, M. M. Salah and M. Mousa, Proposal and design of organic/CIGS tandem solar cell: Unveiling optoelectronic approaches for enhanced photovoltaic performance, *Optik*, 2024, **302**, 171719, DOI: 10.1016/j.ijleo.2024.171719.

27 M. Casademont-Viñas, D. Capolat, A. Quesada-Ramírez, M. Reinfelds, G. Trimmel, M. Sanviti, J. Martín, A. R. Goñi, T. Kirchartz and M. Campoy-Quiles, Combinatorial screening of wide band-gap organic solar cell materials with open-circuit voltage between 1.1 and 1.4 V, *J. Mater. Chem. A*, 2024, **12**, 16716–16728, DOI: 10.1039/d4ta01944j.

28 M. Noman, M. Shahzaib, S. T. Jan, Z. Khan, M. Ismail and A. D. Khan, Optimizing band gap, electron affinity, & carrier mobility for improved performance of formamidinium lead tri-iodide perovskite solar cells, *J. Mater. Sci. Eng. B*, 2024, **300**, 117114, DOI: 10.1016/j.mseb.2023.117114.

29 N. Ahmad, L. Yanxun, X. Zhang, B. Wang, Y. Zhang and H. Zhou, A biopolymeric buffer layer improves device efficiency and stability in inverted organic solar cells, *J. Mater. Chem. C*, 2020, **8**, 15795–15803, DOI: 10.1039/d0tc03048a.

30 A. Kumaresan, S. Yang, K. Zhao, N. Ahmad, J. Zhou, Z. Zheng, Y. Zhang, Y. Gao, H. Zhou and Z. Tang, Facile development of CoAl-LDHs/RGO nanocomposites as photocatalysts for efficient hydrogen generation from water splitting under visible-light irradiation, *Inorg. Chem. Front.*, 2019, **6**, 1753–1760, DOI: 10.1039/c9qi00307j.

31 M. H. Tahir, M. A. A. Ibrahim, S. R. M. Sayed, D. Magero and A. Pembere, Dielectric constant prediction of polymers for organic solar cells and generation of library of new organic compounds, *J. Solid State Chem.*, 2025, **345**, 125213, DOI: 10.1016/j.jssc.2025.125213.

32 Y. Zhang, Y. He, L. Zeng, L. Lüer, W. Deng, Y. Chen, J. Zhou, Z. Wang, C. J. Brabec, H. Wu, Z. Xie and C. Duan, Unraveling the Role of Non-Fullerene Acceptor with High Dielectric Constant in Organic Solar Cells, *Small*, 2023, **19**, 2302314, DOI: 10.1002/smll.202302314.

33 M. R. Khan and B. Jarząbek, Parametric Optimization of High-Dielectric Organic Thin-Film Solar Cells, *Mater. Proc.*, 2024, **17**(16), DOI: 10.3390/materproc2024017016.

34 A. M. Mir, F. Bashir, F. A. Khanday, F. Zahoor, M. Hanif and Z. May, Design and Optimization of High Performance P3HT: PCBM Polymer Solar Cell Using P3HT Buffer Layer, *IEEE Access*, 2024, **12**, 10961–10969, DOI: 10.1109/ACCESS.2024.3354163.

35 M. C. Scharber and N. S. Sariciftci, Efficiency of bulk-heterojunction organic solar cells, *Prog. Polym. Sci.*, 2013, **38**, 1929–1940, DOI: 10.1016/j.progpolymsci.2013.05.001.

36 G. Z. Liu, C. S. Du, J. Y. Wu, B. T. Liu, T. M. Wu, C. F. Huang and R. H. Lee, Enhanced photovoltaic properties of perovskite solar cells by employing bathocuproine/hydrophobic polymer films as hole-blocking/electron-transporting interfacial layers, *Polymers*, 2021, **13**, 42, DOI: 10.3390/polym13010042.

37 R. Po, C. Carbonera, A. Bernardi and N. Camaioni, The role of buffer layers in polymer solar cells, *Energy Environ. Sci.*, 2011, **4**, 285–310, DOI: 10.1039/c0ee00273a.

38 Y. Xia and S. Dai, Review on applications of PEDOTs and PEDOT:PSS in perovskite solar cells, *J. Mater. Sci.: Mater. Electron.*, 2021, **32**, 12746–12757, DOI: 10.1007/s10854-020-03473-w.

39 Y. Liu, Q. Tao, Y. Jin, X. Liu, H. Sun, A. El Ghazaly, S. Fabiano, Z. Li, J. Luo, J. Rosen and F. Zhang, Mo1.33C MXene-assisted PEDOT:PSS hole transport layer for high-performance bulk-heterojunction polymer solar cells, *ACS Appl. Electron. Mater.*, 2020, **2**, 163–169, DOI: 10.1021/acsaelm.9b00668.

40 J. P. Chen, T. W. Colburn, J. Risner-Jamtgaard, A. Vailionis, A. Barnum, M. Golding, A. Carbone, A. C. Flick and R. H. Dauskardt, Open-air spray deposition of PCBM/BCP electron transport layer for inverted perovskite solar cells, *Matter*, 2025, **8**(3), DOI: 10.1016/j.matt.2025.101990.

41 W. Li, G. Wang, Y. Long, L. Xiao, Z. Zhong, X. Li, H. Xu, H. Yan and Q. Song, BCP Buffer Layer Enables Efficient and Stable Dopant-Free P3HT Perovskite Solar Cells, *ACS Appl. Mater. Interfaces*, 2024, **16**, 63019–63025, DOI: 10.1021/acsami.4c15050.

42 P. Peumans, V. Bulović and S. R. Forrest, Efficient photon harvesting at high optical intensities in ultrathin organic double-heterostructure photovoltaic diodes, *Appl. Phys. Lett.*, 2000, **76**, 2650–2652, DOI: 10.1063/1.126433.

43 D. F. O'Brien, M. A. Baldo, M. E. Thompson and S. R. Forrest, Improved energy transfer in electrophosphorescent devices, *Appl. Phys. Lett.*, 1999, **74**, 442–444, DOI: 10.1063/1.123055.

44 H. Yoshida, Electron Transport in Bathocuproine Interlayer in Organic Semiconductor Devices, *J. Phys. Chem. C*, 2015, **119**, 24459–24464, DOI: 10.1021/acs.jpcc.5b07548.

45 G. Shi, J. Yuan, X. Huang, Y. Lu, Z. Liu, J. Peng, G. Ding, S. Shi, J. Sun, K. Lu, H. Q. Wang and W. Ma, Combinative Effect of Additive and Thermal Annealing Processes Delivers High Efficiency All-Polymer Solar Cells, *J. Phys. Chem. C*, 2015, **119**, 25298–25306, DOI: 10.1021/acs.jpcc.5b08861.

46 H. Xu, H. Ohkita, T. Hirata, H. Benten and S. Ito, Near-IR dye sensitization of polymer blend solar cells, *Polymer*, 2014, **55**, 2856–2860, DOI: 10.1016/j.polymer.2014.04.045.

47 R. Zhang, H. Yang, K. Zhou, J. Zhang, X. Yu, J. Liu and Y. Han, Molecular Orientation and Phase Separation by Controlling Chain Segment and Molecule Movement in P3HT/N2200 Blends, *Macromolecules*, 2016, **49**, 6987–6996, DOI: 10.1021/acs.macromol.6b01526.

48 W. J. Huang, S. A. De Valle, J. B. Kana Kana, K. Simmons-Potter and B. G. Potter, Integration of CdTe-ZnO nanocomposite thin films into photovoltaic devices, *Sol.*

Energy Mater. Sol. Cells, 2015, **137**, 86–92, DOI: 10.1016/j.solmat.2015.01.028.

49 C. Bendenia, H. Merad-Dib, S. Bendenia, G. Bessaha and B. Hadri, Theoretical study of the impact of the D/A system polymer and anodic interfacial layer on inverted organic solar cells (BHJ) performance, *Opt. Mater.*, 2021, **121**, 111588, DOI: 10.1016/j.optmat.2021.111588.

50 B. Minnaert and M. Burgelman, Empirical study of the characteristics of current-state organic bulk heterojunction solar cells, *EPJ Appl. Phys.*, 2007, **38**, 111–114, DOI: 10.1051/epjap:2007062.

51 M. K. Hossain, M. H. K. Rubel, G. F. I. Toki, I. Alam, M. F. Rahman and H. Bencherif, Effect of Various Electron and Hole Transport Layers on the Performance of CsPbI3-Based Perovskite Solar Cells: A Numerical Investigation in DFT, SCAPS-1D, and wxAMPS Frameworks, *ACS Omega*, 2022, **7**, 43210–43230, DOI: 10.1021/acsomega.2c05912.

52 P. G. D. K. Ngue, A. T. Ngoupo, A. M. N. Abena, F. X. A. Abega and J. M. B. Ndjaka, Investigation of the Performance of a Sb2S3-Based Solar Cell with a Hybrid Electron Transport Layer (h-ETL): A Simulation Approach Using SCAPS-1D Software, *Int. J. Photoenergy*, 2024, **2024**, 5188636, DOI: 10.1155/2024/5188636.

53 A. T. Ngoupo, S. Ouédraogo, F. Zougmoré and J. M. B. Ndjaka, Numerical analysis of ultrathin Sb2Se3-based solar cells by SCAPS-1D numerical simulator device, *Chin. J. Phys.*, 2021, **70**, 1–13, DOI: 10.1016/j.cjph.2020.12.010.

54 J. C. Zepeda Medina, E. Rosendo Andrés, C. Morales Ruíz, E. Camacho Espinosa, L. Treviño Yarce, R. Galeazzi Isasmendi, R. Romano Trujillo, G. García Salgado, A. Coyopol Solis, F. G. Nieto Caballero and A. C. Carranza Sanchez, Performance simulation of solar cell based on AZO/CdTe heterostructure by SCAPS 1D software, *Heliyon*, 2023, **9**(3), DOI: 10.1016/j.heliyon.2023.e14547.

55 M. Burgelman, K. Decock, A. Niemegeers, J. Verschraegen and S. Degrave, *SCAPS manual*.

56 O. Ahmad, A. Rashid, M. W. Ahmed, M. F. Nasir and I. Qasim, Performance evaluation of Au/p-CdTe/Cs2TiI6/n-TiO2/ITO solar cell using SCAPS-1D, *Opt. Mater.*, 2021, **117**, 111105, DOI: 10.1016/j.optmat.2021.111105.

57 M. P. Hughes, K. D. Rosenthal, N. A. Ran, M. Seifrid, G. C. Bazan and T. Q. Nguyen, Determining the Dielectric Constants of Organic Photovoltaic Materials Using Impedance Spectroscopy, *Adv. Funct. Mater.*, 2018, **28**, 1801542, DOI: 10.1002/adfm.201801542.

58 T. J. K. Brenner, I. Hwang, N. C. Greenham and C. R. McNeill, Device physics of inverted all-polymer solar cells, *J. Appl. Phys.*, 2010, **107**(11), DOI: 10.1063/1.3371364.

59 R. K. Khisamov, A. A. Kistanov, K. S. Nazarov, R. U. Shayakhmetov, G. F. Korznikova, Y. M. Yumaguzin, S. V. Dmitriev and R. R. Mulyukov, Work function of chemical compounds of aluminum-magnesium system, *IOP Conf. Ser.:Mater. Sci. Eng.*, 2020, 012032, DOI: 10.1088/1757-899X/1008/1/012032.

60 P. K. Biswas, A. De, L. K. Dua and L. Chkoda, Work function of sol-gel indium tin oxide (ITO) films on glass, *Appl. Surf. Sci.*, 2006, **253**, 1953–1959, DOI: 10.1016/j.apsusc.2006.03.042.

61 W. Abdelaziz, A. Shaker, M. Abouelatta and A. Zekry, Possible efficiency boosting of non-fullerene acceptor solar cell using device simulation, *Opt. Mater.*, 2019, **91**, 239–245, DOI: 10.1016/j.optmat.2019.03.023.

62 E. Akoto, V. Isahi, V. Odari, C. Maghanga and F. Nyongesa, Monolith Cs1-xRbxSnI3 perovskite – silicon 2T tandem solar cell using SCAPS-1D, *Results Opt.*, 2023, **12**, 100470, DOI: 10.1016/j.rio.2023.100470.

63 P. D. Cunningham and L. Michael Hayden, Carrier dynamics resulting from above and below gap excitation of P3HT and P3HT/PCBM investigated by optical-pump terahertz-probe spectroscopy, *J. Phys. Chem. C*, 2008, **112**, 7928–7935, DOI: 10.1021/jp711827g.

64 Z. Chen, Y. Zheng, H. Yan and A. Facchetti, Naphthalenedicarboximide- *vs.* perylenedicarboximide-based copolymers. synthesis and semiconducting properties in bottom-gate N-channel organic transistors, *J. Am. Chem. Soc.*, 2009, **131**, 8–9, DOI: 10.1021/ja805407g.

65 S. H. Park, Y. Kim, N. Y. Kwon, Y. W. Lee, H. Y. Woo, W. S. Chae, S. Park, M. J. Cho and D. H. Choi, Significantly Improved Morphology and Efficiency of Nonhalogenated Solvent-Processed Solar Cells Derived from a Conjugated Donor–Acceptor Block Copolymer, *Advanced Science*, 2020, **7**, 1902470, DOI: 10.1002/advs.201902470.

66 P. Srivastava, S. Rai, P. Lohia, D. K. Dwivedi, H. Qasem, A. Umar, S. Akbar, H. Algadi and S. Baskoutas, Theoretical study of perovskite solar cell for enhancement of device performance using SCAPS-1D, *Phys. Scr.*, 2022, **97**, 125004, DOI: 10.1088/1402-4896/ac9dc5.

67 M. N. Uddin and P. Afrin, Comparative performance analysis of poly (3-hexylthiophene-2, 5-dial) and [6,6]-phenyl-C61 butyric acid methyl ester-based organic solar cells in bulk-heterojunction and bilayer structure using SCAPS, *Optik*, 2024, **302**, 171691, DOI: 10.1016/j.ijleo.2024.171691.

68 H. Yan, Z. Chen, Y. Zheng, C. Newman, J. R. Quinn, F. Dötz, M. Kastler and A. Facchetti, A high-mobility electron-transporting polymer for printed transistors, *Nature*, 2009, **457**, 679–686, DOI: 10.1038/nature07727.

69 M. S. Yagoub and M. Adnane, Numerical study of P3HT-based hybrid solid-state quantum dot solar cells with CdS quantum dots employing different metal oxides using SCAPS-1D, *Rev. Mex. Fis.*, 2024, **70**, 1–13, DOI: 10.31349/RevMexFis.70.061001.

70 V. Skrypnychuk, G. J. A. H. Wetzelaer, P. I. Gordiichuk, S. C. B. Mannsfeld, A. Herrmann, M. F. Toney and D. R. Barbero, Ultrahigh Mobility in an Organic Semiconductor by Vertical Chain Alignment, *Adv. Mater.*, 2016, **28**, 2359–2366, DOI: 10.1002/adma.201503422.

71 J. Li, J. Du, J. Xu, H. L. W. Chan and F. Yan, The influence of gate dielectrics on a high-mobility n-type conjugated

polymer in organic thin-film transistors, *Appl. Phys. Lett.*, 2012, **100**(3), DOI: 10.1063/1.3678196.

72 G. J. A. H. Wetzelaer, M. Kuik, Y. Olivier, V. Lemaur, J. Cornil, S. Fabiano, M. A. Loi and P. W. M. Blom, Asymmetric electron and hole transport in a high-mobility n-type conjugated polymer, *Phys. Rev. B:Condens. Matter Mater. Phys.*, 2012, **86**, 165203, DOI: 10.1103/PhysRevB.86.165203.

73 P. Kumari, U. Punia, D. Sharma, A. Srivastava and S. K. Srivastava, Enhanced Photovoltaic Performance of PEDOT:PSS/Si Heterojunction Solar Cell with ZnO BSF Layer: A Simulation Study using SCAPS-1D, *Silicon*, 2023, **15**, 2099–2112, DOI: 10.1007/s12633-022-02163-y.

74 E. L. Meyer, S. A. Mvokwe, O. O. Oyedeji, N. Rono and M. A. Agoro, Computational Study of Chalcogenide-Based Perovskite Solar Cell Using SCAPS-1D Numerical Simulator, *Materials*, 2025, **18**, 186, DOI: 10.3390/ma18010186.

75 J. a. Jiménez Tejada, P. López Varo, O. Marinov and M. J. Deen, (Invited) Role of the Metal-Organic Interfaces in the Dark Current-Voltage Characteristics of Organic Solar Cells, *ECS Meeting Abstracts MA2015-01*, 2015, 1259–1259, DOI: 10.1149/ma2015-01/18/1259.

76 S. T. Omelchenko, Y. Tolstova, H. A. Atwater and N. S. Lewis, Excitonic effects in photovoltaic materials with large exciton binding energies, in *2017 IEEE 44th Photovoltaic Specialist Conference, PVSC 2017*, 2017, DOI: 10.1109/PVSC.2017.8366860.

77 S. Rabhi, G. M. Alsulaim, Y. I. Bouderbala and M. W. Alam, Enhancing inverted perovskite solar cells: The role of o-OMe-PEAI interlayer in performance with MXene as alternative front contacts, *Inorg. Chem. Commun.*, 2025, **175**, 114096, DOI: 10.1016/j.inoche.2025.114096.

78 G. Yu, J. Gao, J. C. Hummelen, F. Wudl and A. J. Heeger, Polymer photovoltaic cells: Enhanced efficiencies *via* a network of internal donor-acceptor heterojunctions, *Science*, 1995, **270**, 1789, DOI: 10.1126/science.270.5243.1789.

79 G. Li, R. Zhu and Y. Yang, Polymer solar cells, *Nat. Photonics*, 2012, **6**, 153–161, DOI: 10.1038/nphoton.2012.11.

80 N. I. M. Ibrahim, A. M. Elharbi and A. Albadri, Study the Effect of Thickness on the Performance of PM6:Y6 Organic Solar Using SCAPS Simulation, *Adv. Mater. Phys. Chem.*, 2024, **14**, 55–65, DOI: 10.4236/ampc.2024.144005.

81 M. Lenes, V. D. Mihailetchi, L. J. A. Koster and P. W. M. Blom, Space-charge formation in thick MDMO-PPV:PCBM solar cells, in *Organic Optoelectronics and Photonics II*, 2006, pp. 459–456, DOI: 10.1117/12.664957.

82 M. Lenes, L. J. A. Koster, V. D. Mihailetchi and P. W. M. Blom, Thickness dependence of the efficiency of polymer:fullerene bulk heterojunction solar cells, *Appl. Phys. Lett.*, 2006, **88**, 24, DOI: 10.1063/1.2211189.

83 Y. Kinoshita, R. Takenaka and H. Murata, Independent control of open-circuit voltage of organic solar cells by changing film thickness of MoO3 buffer layer, *Appl. Phys. Lett.*, 2008, **92**, 24, DOI: 10.1063/1.2949321.

84 G. Li, V. Shrotriya, J. Huang, Y. Yao, T. Moriarty, K. Emery and Y. Yang, High-efficiency solution processable polymer photovoltaic cells by self-organization of polymer blends, *Nat. Mater.*, 2005, **4**, 864–868, DOI: 10.1038/nmat1500.

85 G. D. Obikoya, A. Soman, U. K. Das and S. S. Hegedus, Investigation into fill factor and open-circuit voltage degradations in silicon heterojunction solar cells under accelerated life testing at elevated temperatures, *Sol. Energy Mater. Sol. Cells*, 2023, **263**, 112586, DOI: 10.1016/j.solmat.2023.112586.

86 W. Zou, Y. Sun, L. Sun, X. Wang, C. Gao, D. Jiang, J. Yu, G. Zhang, H. Yin, R. Yang, H. Zhu, H. Chen and K. Gao, Extending Exciton Diffusion Length *via* an Organic-Metal Platinum Complex Additive for High-Performance Thick-Film Organic Solar Cells, *Adv. Mater.*, 2025, **37**, 2413125, DOI: 10.1002/adma.202413125.

87 H. J. Park, J. Y. Lee, T. Lee and L. J. Guo, Advanced Heterojunction Structure of Polymer Photovoltaic Cell Generating High Photocurrent with Internal Quantum Efficiency Approaching 100, *Adv. Energy Mater.*, 2013, **3**, 1135–1142, DOI: 10.1002/aenm.201300245.

88 C. Chen, F. Wu, H. Geng, W. Shen and M. Wang, Analytical model for the photocurrent-voltage characteristics of bilayer MEH-PPV/TiO2 photovoltaic devices, *Nanoscale Res. Lett.*, 2011, **6**, 350, DOI: 10.1186/1556-276X-6-350.

89 Y. Kawasugi, K. Seki, Y. Edagawa, Y. Sato, J. Pu, T. Takenobu, S. Yunoki, H. M. Yamamoto and R. Kato, Electron-hole doping asymmetry of Fermi surface reconstructed in a simple Mott insulator, *Nat. Commun.*, 2016, **7**, 12356, DOI: 10.1038/ncomms12356.

90 G. G. Njema, A. Elmelouky, E. L. Meyer and J. K. Kibet, Simulated photovoltaic performance of N719 ruthenium dye sensitised solar cell with a power conversion efficiency exceeding 26% based on electron transport double layer, *RSC Adv.*, 2025, **15**, 44467–44485, DOI: 10.1039/d5ra06604b.

91 P. R. Jubu, Z. S. Mbalaha, E. V. Tikyaa, O. S. Obaseki, K. O. Ighodalo, O. Adedokun, A. Nathan-Abutu, M. B. Ochang, Y. Yusof and M. Z. Pakhuruddin, High-efficiency hole transport layer-free perovskite solar cells utilizing TiO2, ZnO and bilayer TiO2/ZnO electron transport layers: A simulation approach, *Next Mater.*, 2025, **9**, 101166, DOI: 10.1016/j.nxmate.2025.101166.

92 S. Rabhi, L. Hafaifa, O. H. Alsalmi and A. S. Alali, Boosting bifacial efficiency in inverted perovskite solar cells: 95% bifaciality and 28% PCE through materials and device engineering, *New J. Chem.*, 2025, **49**, 13876–13887, DOI: 10.1039/d5nj02604k.

93 H. Elfarri, M. Bouachri, A. Frimane, M. Fahoume, O. Daoudi and M. Battas, Optimization of simulations of thickness layers, temperature and defect density of CIS based solar cells, with SCAPS-1D software, for photovoltaic application, *Chalcogenide Lett.*, 2021, **18**, 201–213, DOI: 10.15251/CL.2021.184.201.

94 M. A. Rahman, Design and simulation of a high-performance Cd-free Cu2SnSe3 solar cells with SnS electron-blocking hole transport layer and TiO2 electron

transport layer by SCAPS-1D, *SN Appl. Sci.*, 2021, **3**, 253, DOI: 10.1007/s42452-021-04267-3.

95 T. Li, L. Jia, W. Zheng and F. Huang, Fermi-Surface Modulation of Graphene Synergistically Enhances the Open-Circuit Voltage and Quantum Efficiency of Photovoltaic Solar-Blind Ultraviolet Detectors, *J. Phys. Chem. Lett.*, 2021, **12**, 11106–11113, DOI: 10.1021/acs.jpclett.1c03279.

96 S. Yalamanchili, N. S. Lewis and H. A. Atwater, Role of Doping Dependent Radiative and Non-radiative Recombination in Determining the Limiting Efficiencies of Silicon Solar Cells, in *2018 IEEE 7th World Conference on Photovoltaic Energy Conversion (WCPEC) (A Joint Conference of 45th IEEE PVSC, 28th PVSEC & 34th EU PVSEC)*, IEEE, 2018, pp. 3223–3226, DOI: 10.1109/PVSC.2018.8547758.

97 S. Dey, M. Paul, S. Porwal, S. K. Varshney and T. Singh, Exploring the Effect of Nonideal Conditions in Perovskite Solar Cells Performance Using Numerical Simulations, *Phys. Status Solidi A*, 2025, **222**, 2400918, DOI: 10.1002/pssa.202400918.

98 A. Bouziane, H. El Ghazi, R. En-nadir, W. Belaid, H. Abboudi and A. Sali, Effects of Doping, Transport Layer Thickness, and Composition on the Performance of Mixed Halide Perovskite Single-Junction Solar Cells, *J. Electron. Mater.*, 2025, **54**, 7296–7307, DOI: 10.1007/s11664-025-12093-1.

99 H. Movla, A. Shahalizad and A. Asgari, A numerical study on the relationship between the doping and performance in P3HT:PCBM organic bulk heterojunction solar cells, *Sci. Rep.*, 2023, **13**, 2031, DOI: 10.1038/s41598-023-29291-8.

100 S. Rabhi, A. BaQais, S. Sadaf and M. W. Alam, Unlocking high efficiency and superior bifacial performance in semi-transparent inverted perovskite solar cells: harnessing MXene and innovative materials for next-generation energy devices, *Surf. Interfaces*, 2025, **73**, 107439, DOI: 10.1016/j.surfin.2025.107439.

101 A. Afaq, D. Pathak, M. Aamir, S. Aziz, Z. Butt, J. Akhtar and T. Akhtar, Low Bandgap Organic Semiconductors for Photovoltaic Applications, *Int. J. Nanosci.*, 2024, **23**, 2430003, DOI: 10.1142/S0219581X24300037.

102 V. Yadav, R. Pandey and N. Shrivastav, Examination of the Total Defect Density and Thickness of CIGS Based PV cell through the SCAPS-1D, in *2024 First International Conference on Electronics, Communication and Signal Processing (ICECSP)*, 2024, pp. 1–4, DOI: 10.1109/ICECSP61809.2024.10698654.

103 S. Rawat, J. Madan and R. Pandey, Exploring the Efficiency of CsSnCl3Perovskite Solar Cells: An Analysis of Absorber Layer Thickness and Defect Density Using 1D-SCAPS Tool, in *ViTECoN 2023 - 2nd IEEE International Conference on Vision towards Emerging Trends in Communication and Networking Technologies, Proceedings*, 2023, DOI: 10.1109/ViTECoN58111.2023.10157560.

104 B. Sopori, V. Budhraja, P. Rupnowski, S. Johnston, N. Call, H. Moutinho and M. Al-Jassim, Defect clusters in multicrystalline silicon: their nature and influence on the solar cell performance, in *Conference Record of the IEEE Photovoltaic Specialists Conference*, 2009, DOI: 10.1109/PVSC.2009.5411527.

105 R. Shubham, C. Pathak and S. K. Pandey, Design, Performance, and Defect Density Analysis of Efficient Eco-Friendly Perovskite Solar Cell, *IEEE Trans. Electron Devices*, 2020, **67**, 2837–2843, DOI: 10.1109/TED.2020.2996570.

106 S. Rabhi, T. Hidouri, S. Goumri-Said, H. J. Alathlawi, G. M. Alsulaim and M. Waqas Alam, Bifacial perovskite solar cells with >21% efficiency: Computational insights into novel HTLs materials and architectures, *Sol. Energy*, 2024, **284**, 113083, DOI: 10.1016/j.solener.2024.113083.

107 K. S. Nithya and K. S. Sudheer, Device modelling of non-fullerene organic solar cell with inorganic CuI hole transport layer using SCAPS 1-D, *Optik*, 2020, **217**, 164790, DOI: 10.1016/j.ijleo.2020.164790.

108 A. Verma, N. Shrivastav and J. Madan, Enhancing Efficiency in Lead-Free Perovskite Solar Cells: The Role of Interface Defect Density in FAMASnGeI$_3$ Device, in *2024 Global Conference on Communications and Information Technologies (GCCIT)*, IEEE, 2024, pp. 1–5, DOI: 10.1109/GCCIT63234.2024.10862759.

109 L. Antwi and S. Huang, Defect State Dynamics in Lead-Free Perovskite Solar Cells for Enhanced Efficiency, *Int. J. Mater. Sci. Appl.*, 2024, **13**, 113–120, DOI: 10.11648/j.ijmsa.20241306.12.

110 S. Y. Leblebici, T. L. Chen, P. Olalde-Velasco, W. Yang and B. Ma, Reducing exciton binding energy by increasing thin film permittivity: an effective approach to enhance exciton separation efficiency in organic solar cells, *ACS Appl. Mater. Interfaces*, 2013, **5**, 10105–10110, DOI: 10.1021/am402744k.

111 T. Upreti, S. Wilken, H. Zhang and M. Kemerink, Slow Relaxation of Photogenerated Charge Carriers Boosts Open-Circuit Voltage of Organic Solar Cells, *J. Phys. Chem. Lett.*, 2021, **12**, 9874–9881, DOI: 10.1021/acs.jpclett.1c02235.

112 J. Gorenflot, W. Alsufyani, M. Alqurashi, S. H. K. Paleti, D. Baran and F. Laquai, Increasing the Ionization Energy Offset to Increase the Quantum Efficiency in Non-Fullerene Acceptor-Based Organic Solar Cells: How Far Can We Go?, *Adv. Mater. Interfaces*, 2023, **10**, 2202515, DOI: 10.1002/admi.202202515.

113 S. J. Fonash, *Solar cell device physics*, Elsevier, 2012.

114 W. Tress, K. Leo and M. Riede, Optimum mobility, contact properties, and open-circuit voltage of organic solar cells: a drift-diffusion simulation study, *Phys. Rev. B*, 2012, **85**, 155201, DOI: 10.1103/PhysRevB.85.155201.

115 T. A. Mbanga, D. Afungchui, J. Ebobenow, A. Helali and N. A. Arreyndip, Charge carrier mobility and the recombination processes within a bulk heterojunction organic solar cell exhibiting disordered hopping, *J. Renew. Energy*, 2024, **27**, 191–212, DOI: 10.54966/jreen.v27i2.1190.

116 H. Nojima, T. Kobayashi, T. Nagase and H. Naito, Modulated Photocurrent Spectroscopy for Determination of Electron and Hole Mobilities in Working Organic Solar

Cells, *Sci. Rep.*, 2019, **9**, 20346, DOI: 10.1038/s41598-019-56945-3.

117 N. Bouri, H. Diyagh, A. Lemnawar, S. Rabhi, A. Talbi, A. Rmili, T. A. Geleta, S. Amraoui, M. Makha and K. Nouneh, Comparative study of solar cells based on triple and graded absorber layers with the compound CsSn1-xGexI3: Numerical study and optimization, *J. Phys. Chem. Solids*, 2025, **199**, 112561, DOI: 10.1016/j.jpcs.2025.112561.

118 N. Bouri, T. A. Geleta, K. W. Guji, A. Hammad, S. Rabhi and K. Nouneh, Resistance dynamics in a solar cell with novel lead-free perovskite absorbers (LiMgI3 and NaMgI3): performance optimization using SCAPS-1D simulation and impedance spectroscopy, *J. Phys. Chem. Solids*, 2025, **207**, 112972, DOI: 10.1016/j.jpcs.2025.112972.

119 Z. Lucheng, X. Xinxiang, Y. Zhuojian, S. Xiaopu, X. Hongyun, L. Haobin and S. Hui, An efficient method for monitoring the shunts in silicon solar cells during fabrication processes with infrared imaging, *J. Semicond.*, 2009, **30**, 076001, DOI: 10.1088/1674-4926/30/7/076001.

120 S. Fabiano, Z. Chen, S. Vahedi, A. Facchetti, B. Pignataro and M. A. Loi, Role of photoactive layer morphology in high fill factor all-polymer bulk heterojunction solar cells, *J. Mater. Chem.*, 2011, **21**, 5891, DOI: 10.1039/c0jm03405c.